Dissertation
submitted to the
Combined Faculties for the Natural Sciences and for Mathematics
of the Ruperto-Carola University of Heidelberg, Germany
for the degree of
Doctor of Natural Sciences

presented by

Master of Science:	Heiko Eisele
born in:	Stuttgart, Germany

Oral examination: 12/18/2002

Automated defect detection and evaluation in X-ray CT images

Referees:	Prof. Dr. Fred Hamprecht
	Prof. Dr. Kurt Roth

Zusammenfassung

Die Röntgencomputertomographie findet zunehmend Einsatz in der industriellen Qualitätskontrolle. Es ist jedoch eine grosse Herausforderung, sie in der vollautomatisierten Fertigung zu verwenden, da dies u.a. robuste Volumenbildverarbeitung auf verrauschten Bildern erfordert. Die vorliegende Arbeit präsentiert Methoden zur automatischen Detektion und geometrischen Beschreibung von Defekten. Die Erkennung der Defekte beruht auf einer statistischen Grauwertanalyse. Im Anschluss an die Detektion werden defekte Voxel gruppiert um Form und Grösse der zugehörigen Materialfehler zu bestimmen. Es werden Ergebnisse in der Poren- und Rissdetektion von Stahlteilen gezeigt.

Abstract

X-ray computed tomography gains increasing popularity for industrial quality inspection tasks. It is a challenge however to use it in a fully automated assembly line, which requires robust algorithms for volumetric image analysis on noisy data. This work provides methods for the automatic detection of defects and their geometric description. The approach will be based on spatial statistical analysis of the voxel structure to determine the presence of a defect. Once detected, defect voxels will be clustered to determine shape and size of the associated material faults. The effectiveness of the method will be shown on pores and cracks in steel parts.

Table of Contents

1 Introduction

X-ray computerized tomography is a powerful technique to image internal features of industrial parts. It thus attracts the interest of quality control engineers, who otherwise rely on less universal non-destructive testing methods such as ultra-sound or eddy current. In many cases they even have to revert to destructive techniques, which are elaborate and can access internal features at selected positions only. X-ray CT on the other hand generates a volume image of the entire object down to resolutions of a few μm easily achieved with modern systems.

This work contributes to automatic processing of X-ray CT data with the purpose of defect detection. While known techniques in that field primarily have been developed for conventional 2D X-ray imaging [1,2,3,4], this paper provides algorithms, which define pixel neighborhoods in all three coordinate directions.

The report is organized as follows: Section 2 gives a brief overview of typical defect detection tasks approached through X-ray CT. Section 3 discusses previously reported work on related techniques in the field of 2D X-ray image evaluation. We proceed in section 4 with a quick summary of technical aspects of X-ray CT to give some insight into specific challenges faced by image processing. Section 5 puts our work in the context of volume image processing techniques used in other areas such as medical research. Sections 6 and 7 detail the main contributions of this work. Section 6 is concerned with the detection of defects, whereas section 7 provides techniques to extract their features such as size and shape. The main part of this paper concludes in a summary and outlook. We designed a GUI-based software application that serves as an interface to parameterize and apply the algorithms to arbitrary CT-data. We will describe some key aspects of that work in the appendix.

2 Industrial Applications of CT

The detection of pores, contraction cavities, cracks and inclusions are important tasks in industrial quality control. Pores and contraction cavities are material faults found in welds and castings (see fig. 1(a) and (b)). While it is technically often not possible to produce parts free of defects, their type and extent determine whether the part has to be classified as good or bad. In addition, a detailed spatial distribution of the defects obtained through CT provides valuable information for process engineers. A CT-system could be used for mechanically supervised monitoring of the manufacturing process. This requires fully automatic evaluaton of the images which is the objective of this work.

Fig. 1(c) shows a crack running through a steel part. While cracks are the most critical of all defects, they are extremely hard to detect. The visibility of a defect in an X-ray image primarily depends on two factors: the difference in absorption with respect to its environment and its size. Since cracks are very narrow, they offer a minimum of contrast and in many cases can't be resolved at all.

Another class of defects are inclusions. Fig. 1 shows an inclusion that had developed during the welding process. Its contrast is very weak since it consists of slag that has an absorption very similar to the surrounding material.

A further application of industrial X-ray CT is the measurement of inner geometries. However, most current applications can be found in the areas of defect detection discussed in the previous paragraph. For that reason and due to the fact, that defect detection can be approached in a more general manner we chose to focus our efforts on that field.

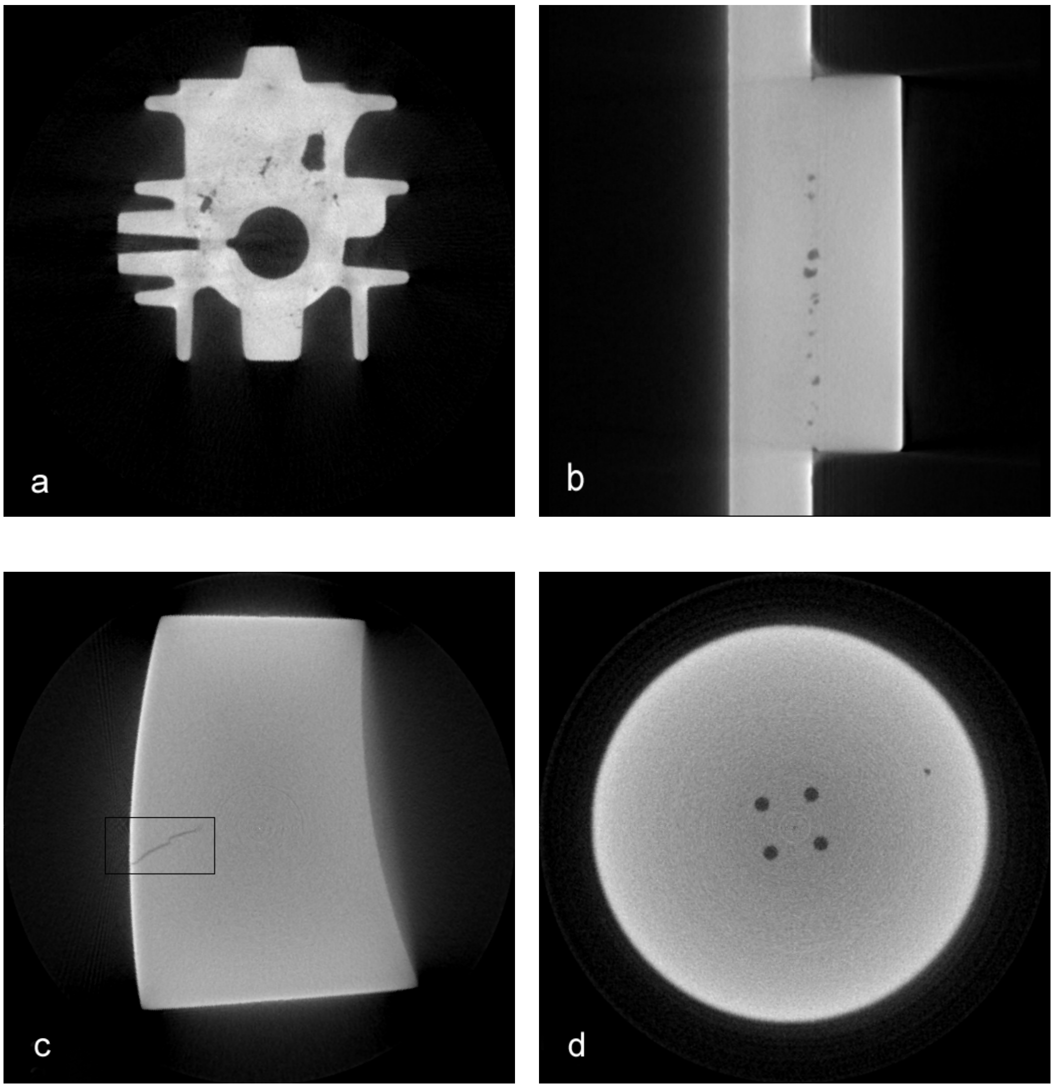

Fig. 1: Examples for industrial inspection tasks. (a) Pores and contraction cavities in castings, (b) and (d) welding defects, (c) crack.

3 Review of related work

Defect detection requires a decision whether individual voxels differ significantly from the background. Early applications have used median filtering techniques to obtain a background image and applied a threshold to the difference image [1]. To distinguish between constructive features and defects, they adapted the filter mask to the object geometry. Each object requires a learning stage in which the best masks are selected either manually or automatically. This requires a defect-free part, however, which is not always available. The mask selection has been improved in [3], but the method still has difficulty with low-contrast defects typical in X-ray CT images (see fig. 4). Gayer et al. [2] used high-pass or first derivative filtering to identify potential defects. True defects were subsequently identified via template matching. This technique takes advantage of neighborhood information but requires a priori knowledge about defect shapes. Alternatively, the authors computed a background image by interpolating between pixels that had been marked as intact and applied a threshold to the difference image. However, this still has the previously mentioned disadvantages, i.e. poor performance on low-contrast noisy defects.

A recent approach uses both spatial variance and spatial contrast and applies fuzzy reasoning to distinguish between defect and background [4]. This technique does not require heuristic threshold parameters since these are estimated in the training process.

Our method will detect defects by evaluating the deviation not of singular voxels, but structural deviations from the background. This approach is particularly suitable for low-contrast planar defects such as cracks, that are difficult to detect with other methods. However, the technique works on more compact defects such as pores and contraction cavities as well.

4 CT Fundamentals

This section gives an outline of the data aquisition process in X-ray CT, i.e. data recording and geometry reconstruction. Data recording refers to the physical collection of data through an X-ray detector whereas reconstruction processes those data to obtain a volume model of the object.

4.1 Data Recording

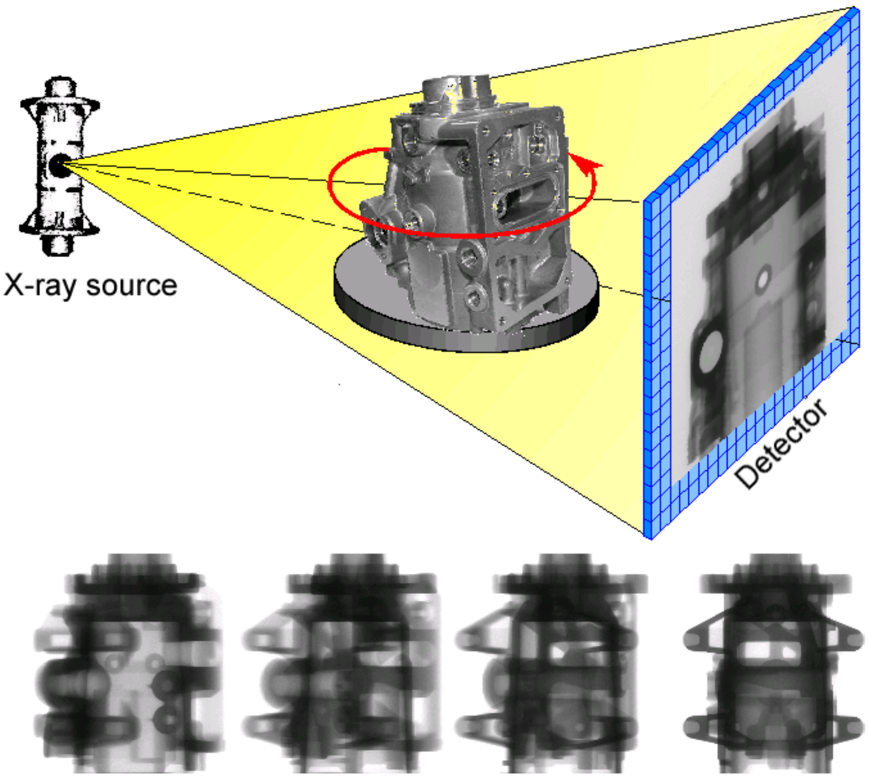

Fig. 2: During a CT recording, several hundred individual images are taken from different angles and used to reconstruct the volume information. Provided by Dr. Andreas Siegle, Robert Bosch Corp.

Fig. 2 illustrates the principle of X-ray CT data recording. An X-ray source irradiates an object whose image is recorded by a detector array. The turntable rotates stepwise to record object images from different angles. A CT recording typically consists of several hundred individual projections.

During image reconstruction, individual images obtained from different angles are processed to yield a 3D volume image of the object. The basic algorithm to perform this task is the so-called Feldkamp-Algorithm [5]. This technique has been modified for increased performance or better image quality in a number of articles, e.g. [6].

4.2 Image Properties

The reconstructed images have a number of properties characteristic of X-ray CT-data. The major challenges image processing algorithms have to cope with are artifacts and noise.

4.2.1 Artifacts We only quote the most salient artifacts that limit defect detection. The so-called *cupping artifacts* make the absorption appear stronger near the boundaries than in the interior of the object, even if it is homogeneous (see fig. 3). We will model defect-free image data based on a local training region. The non-homogeneity caused by the cupping artifact will limit the algorithm's performance near the object boundaries. The physical cause for the cupping artifact lies in the non-linearity of the absorption as a function of the beam energy and is discussed in more detail in [7].

Edge artifacts appear as a halo near the object boundary making small defects difficult to detect, especially close to strongly absorbing materials (fig. 4).

4.2.2 Noise As most defects manifest themselves in a deviation of the absorption from that of homogeneous material, their detectability is limited by noise (see fig. 4). In section 6.3 we will perform defect detection by evaluating the significance of the deviation of groups of pixels from the background. This will involve estimating the covariance matrix

$$Cov_g = \left\langle \left(g_{(i,j,k)} - \bar{g}\right), \left(g_{(i',j',k')} - \bar{g}\right) \right\rangle \tag{1}$$

where we average across the homogeneous area of the image, and subsequently estimate the noise after performing certain neighborhood operations. Details of that procedure including the quantification of the noise parameters will be presented in section 6.3.

4.3 Processing time

Image processing should take no longer than data recording and reconstruction, which require approximately $20 - 30$ min each for a $512 \times 512 \times 512$ volume. The bottleneck in data recording is the integration time on the detector to obtain a sufficiently large signal-to-noise ratio.

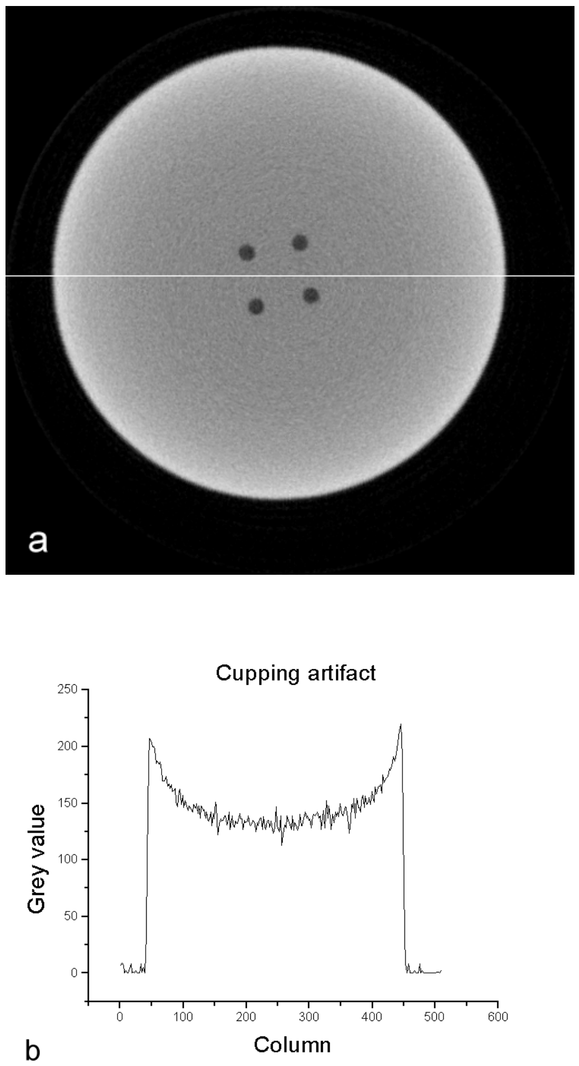

Fig. 3: *Cupping artifact.* The grey values in the middle of the object are smaller even though the X-ray absorption is constant throughout the object. (a) Grey image, (b) cross-section.

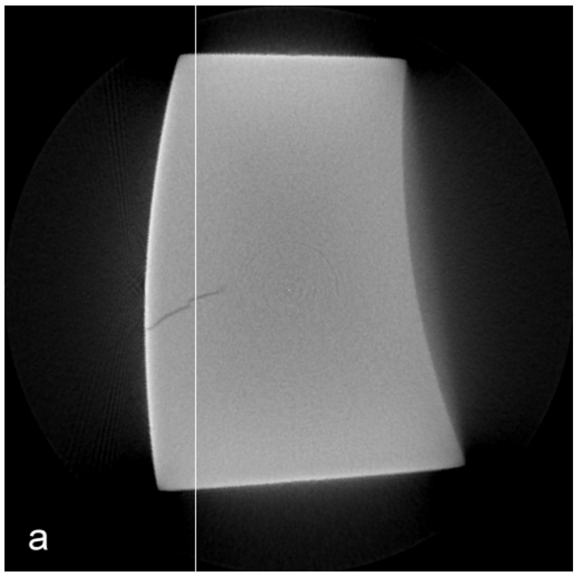

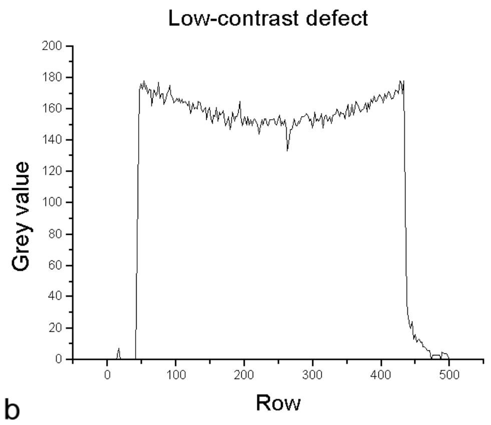

Fig. 4: *Noise.* The crack is hard to detect due to its low contrast. (a) Grey image, (b) cross-section.

5 Volume image processing

Currently most applications of volume image processing can be found in medical fields such as cancer diagnosis or brain research [8,9,10]. This section gives a brief overview of techniques that can also used for industrial image processing.

5.1 Detection

Defect detection means assigning voxels to two kinds of classes: intact or defect. This decision will be based on thresholding techniques which are basically classified as point-dependent or region-dependent. Point-dependent techniques take into account a pixel's grey value only whereas region-dependent methods use neighborhood information. Both techniques may be applied locally or globally [11].

5.1.1 Segmentation Segmentation refers to the process of extracting connected regions with similar properties. This is a common problem in brain research, where the goal is to obtain a functional map of the brain [9,10]. Typical techniques in this field are so-called region growing algorithms, where starting from distinct seed points, regions with similar grey value structure are extracted. We will use this general technique to distinguish between defects and constructive object features.

5.1.2 Feature extraction In feature extraction we will compute parameters describing size and geometric defect properties. Known methods can be divided into two main categories: model-based (parametric) and non-parametric.

An example of non-parametric techniques are active contours or ’snakes’ introduced in [12]. The physical analogy of an active contour is a ring of masses connected by springs. The masses also experience a force derived from a grey image. A common method to calculate this force is to equate the grey value of an image with the potential energy. The snake will then change shape to reach a state of minimum energy. This method has a drawback regarding noisy images: The snake might get stuck in a local minimum. As a solution Velasco et al. introduced so-called Sandwich Snakes [13]. Here two snakes are initialized, one inside and one outside the object. The interaction among them will force them to converge on the true object boundary. Raisch et al. [14] applied a special energy term with reduced noise to avoid being trapped in local minima in the first place.

While snakes are very useful in boundary extraction and have been widely applied, they do not directly yield object features. Model-based approaches yield object properties directly and can be adapted to the desired level of detail. Examples of prototypes are ellipsoids [15] and spherical harmonics [16]. In [16], the use of moments for shape characterization is discussed as well.

In our work we decided to use a model-based approach, since lower order shape parameters are usually sufficient for defect characterization.

5.2 Outline of the main contribution of this work

Section 6 deals with the detection of defect voxels. For an object composed of one material, we first perform a grey value segmentation using a global threshold, which is determined from the histogram. This distinguishes between material and air. In a second step, we use topological properties of the segmented regions to distinguish between defects and background.

In the subsequent section we suggest an alternative to using a global threshold as a criterion for binarization. We apply structure enhancing operators locally and regard defects as outlier structures from the estimated background. As we will show this technique performs better on low-contrast noisy images with varying intensity. In contrast to previously reported approaches, it uses both neighborhood information and subsequent statistical testing for defect detection. The detection threshold can then be chosen independently from the image content.

Section 7 determines the shape characteristics of the defects based on the detection result. We will suggest two model-based approaches: The first one describes defects with ellipsoids. This seems appropriate since in many cases one is interested in the main axes of a defect and their ratios. The second approach uses spherical harmonics, which allows to distinguish among more complex shapes. This model is very flexible in the sense that it can be adapted to the level of shape details one is interested in.

Section 8 recapitulates the key accomplishment of this work, i.e. to generate a defect protocol based on raw CT-data. The main part of this thesis concludes with a summary and some proposals for future work.

6 Defect detection

Defect detection refers to the process of classifying voxels as either intact or defect. We first need to discard all voxels that are not an integral part of the object, such as the air in the environment or in a drillhole. This discrimination is accomplished by means of a threshold, the choice of which is documented in section 6.1. Section 6.2 describes how we distinguish between inclusions and air. Finally, section 6.3 details our attempt how to detect more subtle defects that are not found by a simple thresholding operation.

6.1 Object and background

The simplest possible method for fault detection is to classify each single voxel of the raw image $g(i, j, k)$ as defect or intact according to the following criterion:

– voxel intact if $g_{(i,j,k)} > t$,
– voxel defect if $g_{(i,j,k)} < t$,

where t is some threshold within the dynamic range of the image (0...255 in our examples). In the sense of [11], this method is global point-dependent.

Commonly used threshold selection techniques model the grey value distribution $g(x)$ as a sum of Gaussian components, see (see [11]):

$$f(x) = \sum_i \frac{p_i}{\sigma_i\sqrt{2\pi}} e^{-\frac{(x-m_i)^2}{\sigma_i^2}} \tag{2}$$

A voxel is then assigned to the class with the highest probability density. This technique is known in the literature as mixture density modeling. Known mixture density decomposition algorithms are the MF-Estimator [17,18], and the generalized minimum volume ellipsoid (GMVE) [19]. These techniques estimate the parameters of each cluster by iterative refinement, which is a computationally expensive procedure and might even fail in the case of poorly chosen initial estimates [11]. Chang et al. [11] suggest an alternative approach: Instead of estimating the parameters iteratively, they choose optimal initial conditions by first smoothing the histogram and then finding a window around each peak in which the distribution has zero skewness. The parameters are then estimated in a single step from these intervals. While this algorithm yields better performance and more accurate results than techniques using the MF-Estimator and B-Splines, the authors point out that the results will depend on the size of the filter used for smoothing the histogram (see [20] for a general discussion of B-Splines in computer vision).

In our application, the number of components to be segmented is known a priori since it corresponds to the number of materials with different X-ray absorption (see fig. 6(b)). The leftmost flank of the histogram in fig. 6(b) is typical for X-ray CT-images and arises from artifacts during reconstruction. The main peak comes from the object itself, and the small bump in-between is due to the halo effect described in section (see section 4.2.1). Knowing the desired number of components in advance, we propose an algorithm for automatic threshold selection that does not make any prior assumptions about the particular distribution type. Our method works iteratively but without heuristic input parameters. The histogram is smoothed iteratively with a (3×1) Binomial until the number of local maxima equals the number of material components. The local minima of the histogram are then chosen as thresholds (see fig. 6.1). Once the grey image is binarized at the resulting threshold, we obtain an approximate segmentation of the object, which classifies voxels as either occupied with material or air. This approach works well if the peaks from the different materials are sufficiently distinct such that they do not coalesce. To detect defects we have to further differentiate among those classified as air. This is done by classifying their topology as described in the following section.

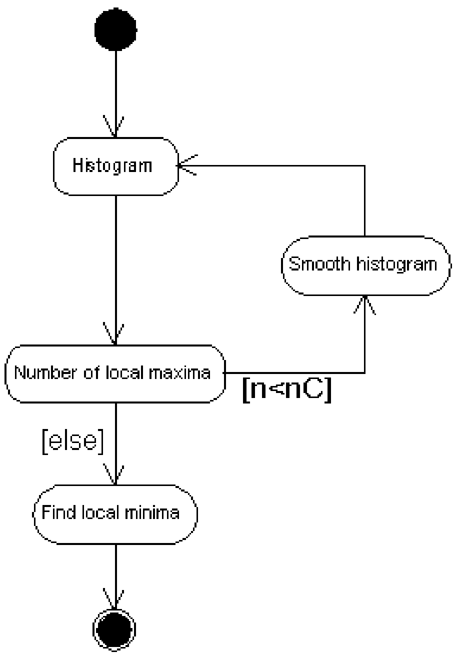

Fig. 5: Iterative histogram smoothing.

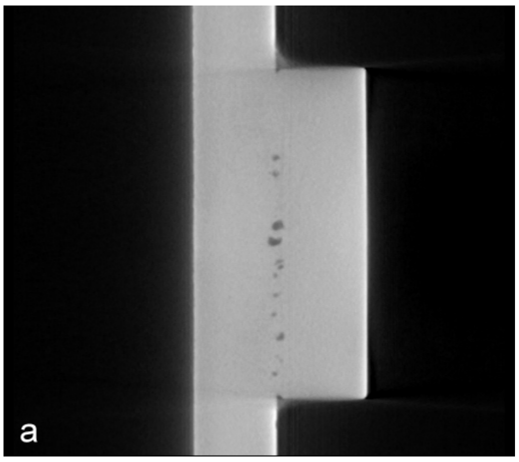
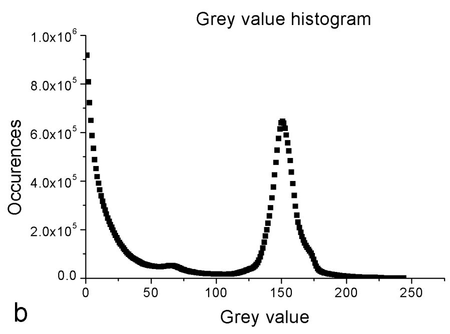

Fig. 6: (a) CT-image of a steel part with defects. (b) Associated histogram.

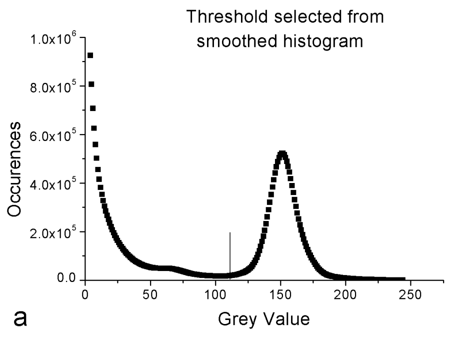

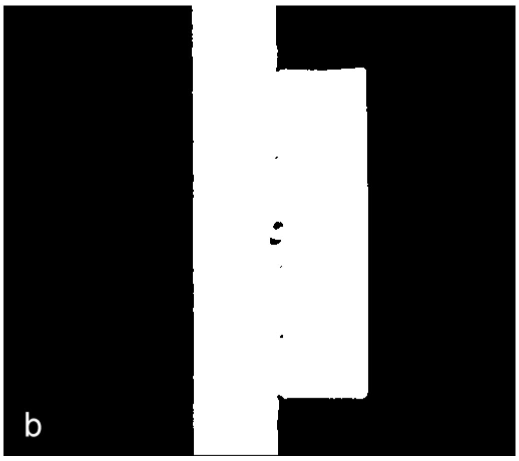

Fig. 7: (a) Smoothed histogram. (b) Fig. 6(a) binarized at the threshold extracted from the smoothed histogram.

6.2 Classifying regions as defect

Consider a single-component image that has been binarized to distinguish between material and air/vacuum (see section 6.1). This assigns both the surrounding background and defects the same class, so we have to apply further techniques to extract the defects. For this purpose we apply a so-called region growing technique commonly used in segmentation. Starting from a seed area, neighboring voxels will be included if the newly created region satifies certain homogeneity criteria based on grey values, color or texture [10,21,22]. Applications are primarily found in medical image registration. [10,9] but also in other areas such as video segmentation [21] or general applications [22].

To outline how to extract the defects in our binarized image of fig. 7(b)we first have to give some definitions:

Definition 1 *Connectivity. Each voxel is connected to those of its 26 nearest neighbors that have the same grey value class.*

Definition 2 *Each connected graph corresponds to one region.*

These definitions allow us to disregard all voxels that are connected to the surrounding atmosphere, such as drillings and channels. All remaining sub-threshold regions are classified as defects. We implement a 3D region growing algorithm that labels regions in the binarized image of fig. 7(b) to extract defects. This algorithm uses the following homogeneity criteria:

$$h = 1 - b_{(i,j,k)}, \tag{3}$$

where $b_{(i,j,k)}$ is the value of the binary image of fig. 7(b) (i.e. 0 or 1). The voxel (i, j, k) will join the region if and only if $h = 1$. Results are shown in fig. 8 and algorithmic details can be found in B.1. A schematic diagram of the detection algorithm discussed can be found in appendix D.

This technique has two limitations: firstly, defects that are just a few voxels in size are often not detected due to their low contrast (fig. 9(b)). Secondly, surface defects cannot be detected since they are labeled as surrounding air (fig. 9(a)).

6.3 Improvements for small low-contrast defects

Applying a global threshold to the image often leaves small or low-contrast defects undetected. In this section, we introduce methods for a local image analysis, that classifies voxels with respect to their neighborhood, rather than globally. This

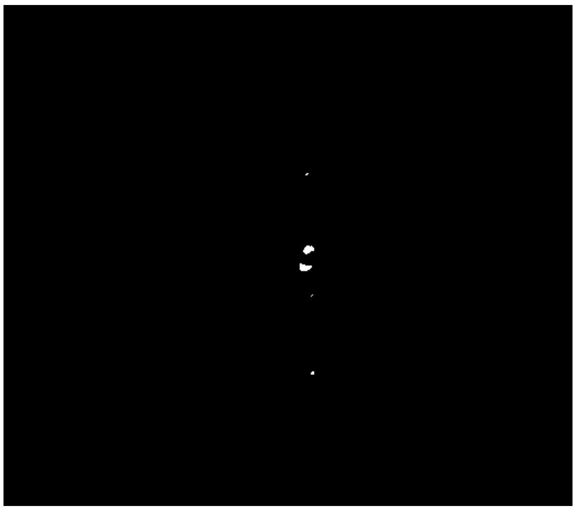

Fig. 8: Fig. 7(b) after the 3D labeling. Defects are objects classified as background that are not connected to the outer image region.

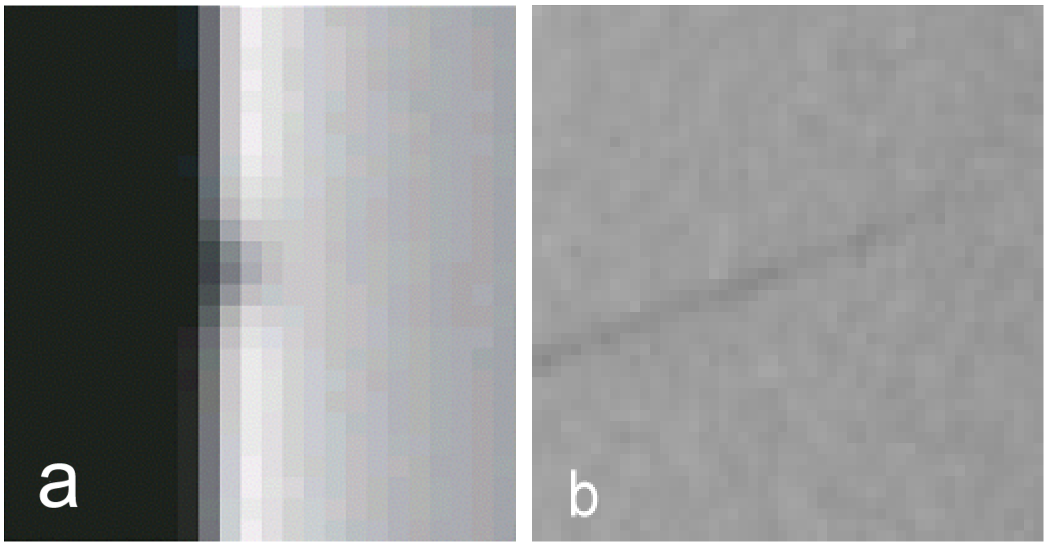

Fig. 9: Examples of defects that usually remain undetected by global thresholding and 3D labeling: (a) surface defects, since they are connected to the outer image region and are thus classified as background and (b) small defects with low contrast such as cracks.

procedure comprises two steps: Firstly, defects are enhanced using special filtering techniques and secondly, a threshold is chosen based on the covariance properties of a defect-free training region.

6.3.1 Defect enhancement The key to defect enhancement is to detect oriented structures within the image. Commonly used techniques are tensorial approaches, which are discussed in [23,24,25,26]. These methods require eigenvalue computation for each pixel, which results in a computationally expensive procedure. In addition, they respond to both edges and noise. As an alternative, we suggest to simply take the square of locally averaged derivatives as an edge detector. This suppresses the noise and, at the same time, enhances pixels within areas of coherent grey value structure. The corresponding operator looks like this:

$$g'(\boldsymbol{x}) = \sum_{i=1}^{3} \left(\int w(\boldsymbol{x} - \boldsymbol{x'}) \frac{\partial g(\boldsymbol{x'})}{\partial x_i} d\boldsymbol{x'} \right)^2 \tag{4}$$

Here $g(\boldsymbol{x'})$ is the grey value at point $\boldsymbol{x} = (x_1, x_2, x_3)$ and $\partial/\partial x_i$ the derivative with respect to the i^{th} coordinate. w denotes a three-dimensional smoothing function (commonly a Gaussian). The discrete version of this equation is

$$g' = (g * f_x^p)^2 + (g * f_y^p)^2 + (g * f_z^p)^2 \tag{5}$$

where

$$\begin{aligned} f_x^p &= B_x^p B_y^p B_z^p D_{2x} S_y S_z \\ f_y^p &= B_x^p B_y^p B_z^p D_{2y} S_x S_z \\ f_z^p &= B_x^p B_y^p B_z^p D_{2z} S_x S_y \end{aligned} \tag{6}$$

The filter masks are

$$\begin{aligned} D_{2x} &= [\ 0.5 \quad 0 \quad -0.5\ ] \\ S_x &= [\ 0.1839155 \quad 0.632169 \quad 0.1839155\ ] \end{aligned} \tag{7}$$

and the binomial filters B_x^p are defined as

$$\begin{aligned} B_x^0 &= [\ 1\ ] \\ B_x^1 &= [\ 1 \quad 1\ ] \\ B_x^2 &= [\ 1 \quad 2 \quad 1\ ] \end{aligned} \tag{8}$$

The filters with index y and z have the same coefficients and are applied in the y and z-direction, respectively. $D_{2x} S_y S_z$ represents a first derivative operator in x-direction that has been optimized for isotropy [27]. Smoothing the image of first derivatives has the effect that areas with coherent linear structure are preserved, whereas noise is suppressed. Results obtained on both artificial and real data will be presented in the following section. For detection, we set a threshold above which we regard a signal as significant. This requires a statistical model and estimating parameters.

6.3.2 Statistical model The noise is correlated as will be shown shortly. We therefore model the absorption $g(x)$ of an intact object as locally homogeneous with added correlated isotropic normal noise. In other words, we interpret the data as realization of a stochastic process with drift (the mean is only locally constant). The covariance structure is assumed constant throughout the random field (homoscedasticity), and it is estimated from a homogeneous training region (see fig. 11.

In fig. 10a CT-data of a defect part have been simulated by adding uncorrelated normal noise to a constant grey image where the voxels of the YZ plane across the center have been set to a lower grey value, and convolving the result with a $(3\times3\times3)$ binomial filter to obtain correlated noise. Fig. 10b shows the result of the filtering with (5). Even though the crack in fig. 10a is clearly visible, the signal across the horizontal cross section through the image hardly shows a significant deviation from the background (fig.10c).

If g denotes the constant grey image with added uncorrelated normal noise σ and if $\tilde{g}$ is obtained from g by convolution with a three-dimensional Binomial $b_{(i,j,k)}$, then the variance $\tilde{\sigma}^2$ of $\tilde{g}$ becomes

$$\tilde{\sigma}^2 = \sigma^2 \sum b^2_{(i,j,k)} \tag{9}$$

where the summation extends over all filter coefficients. For a $(3 \times 3 \times 3)$ binomial filter the variance of the noise in fig. 10a thus becomes

$$\tilde{\sigma}^2 = 0.05273\sigma^2\cdot \tag{10}$$

Fig. 10c illustrates the difficulty in detecting low-contrast defects: A threshold of $3\tilde{\sigma}$ will barely detect the crack and, at the same time, yield a large number of pseudo errors – for a normal distribution $f(x) = \frac{e^{-x^2/(2\sigma^2)}}{\sigma\sqrt{2\pi}}$ we have to expect a false alarm rate of 2.7%. In a typical image with $512 \times 512 \times 512$ voxels more than a million intact voxels would be classified as defect, which is unacceptable. Fig. 10d shows a far better signal-to-noise ratio. To determine an appropriate threshold, we have to know the variance of the noise in the filtered image. The next section will detail how to calculate that noise from the covariance matrix of the source image.

6.3.3 Error Propagation To determine the covariance matrix of the source image we manually select a defect-free homogeneous training region and compute the covariance matrix under the assumption that the noise is isotropic (see fig. 6.3.3). To see the effect of the filtering on the covariance matrix, we rewrite (5) as

$$g' = (g'_x)^2 + (g'_y)^2 + (g'_z)^2 \tag{11}$$

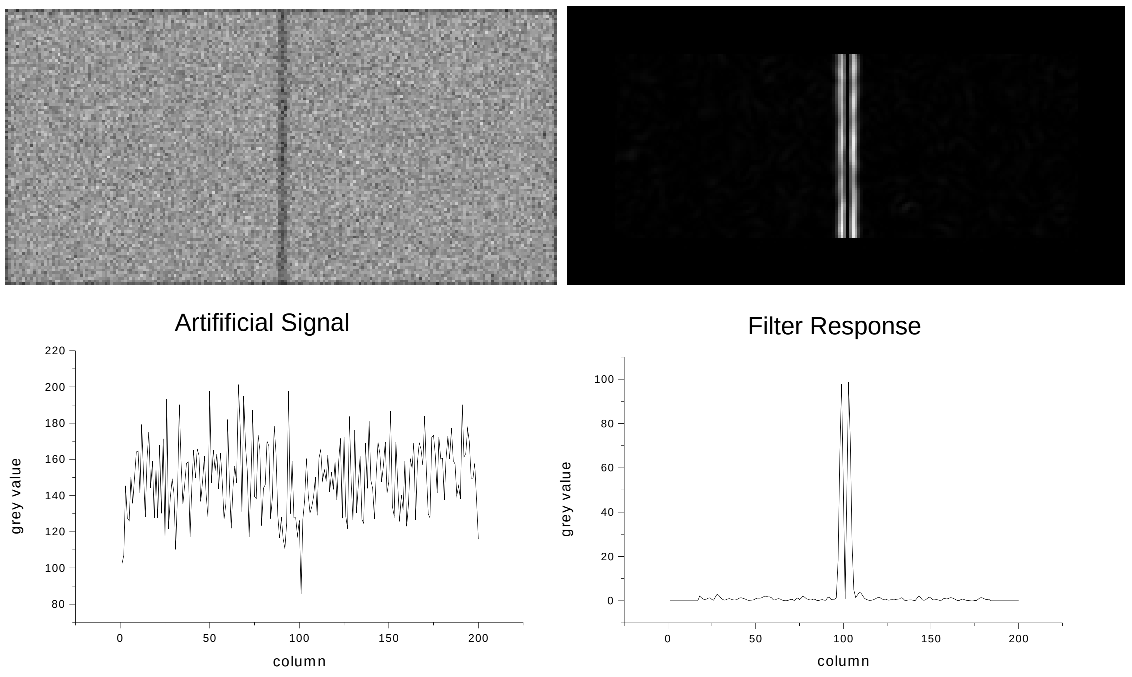

Fig. 10: Effect of the filtering on an artificial 3D image: (a) slice of original image: homogeneous with crack and added correlated noise (white Gaussian noise convolved with a (3 × 3 × 3) binomial filter). (b) Image after it has been filtered with (5); smoothing operator: (13×13×13) binomial filter. (c) Horizontal cross section through the original image and (d) the filtered image.

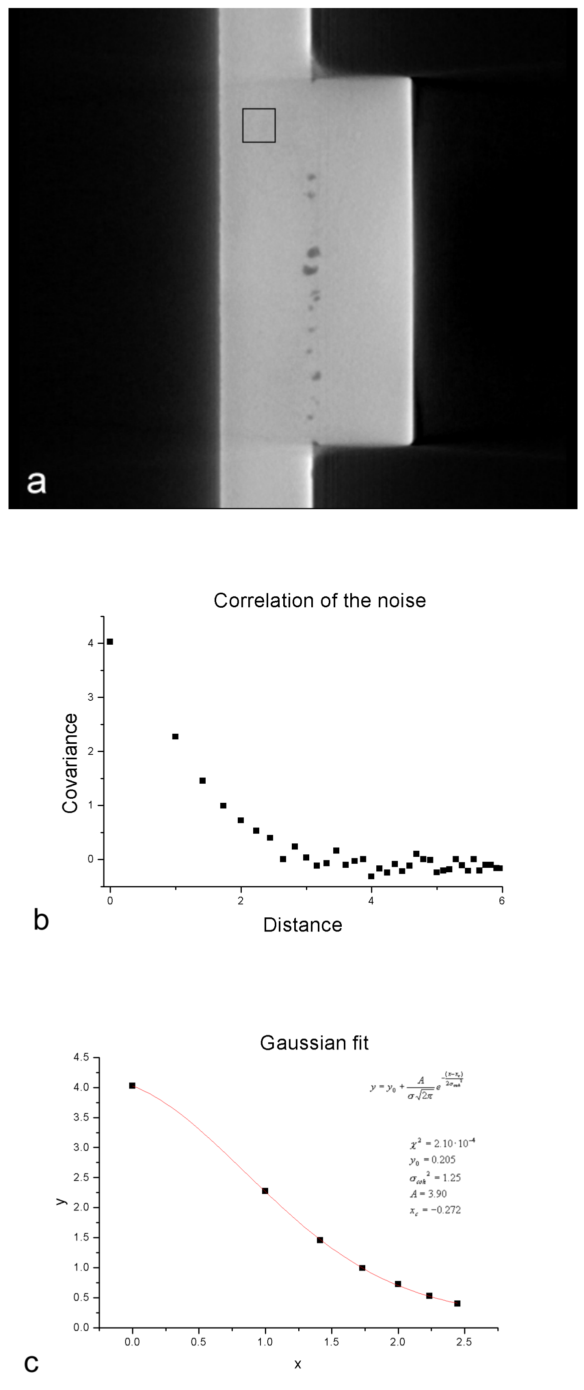

Fig. 11: Analyzing the covariance structure. (a) Original image with hand-selected training region. (b) Empirical covariance vs. distance assuming isotropic noise. (c) A Gaussian fit to the empirical covariance data for small distances has a standard deviation of $\sigma_{coh} = 1.12$.

where

$$g'_x = g * f^p_x, \qquad g'_y = g * f^p_y, \qquad g'_z = g * f^p_z, \tag{12}$$

At point (i, j, k), we obtain

$$g'_{x(i,j,k)} = \sum_{\{l,m,n\}=-r}^{r} f^p_{x(l,m,n)} g_{(i-l,j-m,k-n)}, \tag{13}$$

where $f^p_{x(l,m,n)}$ are the coefficients of our three-dimensional filter f^p_x. If the image is modeled as a random field as described in the previous paragraph, the variance $\sigma'^2_{x(i,j,k)}$ of $g'_{x(i,j,k)}$ is

$$\sigma'^2_{x(i,j,k)} = \mathbb{E}\left[\left(g'_{x(i,j,k)} - \mathbb{E}\left[g'_{x(i,j,k)}\right]\right)^2\right], \tag{14}$$

where $\mathbb{E}$ denotes expectation. We substitute (13) into (14), rearrange terms and compute the expectation value term by term in order to obtain

$$\begin{aligned}\sigma'^2_{x(i,j,k)} = &\sum_{\{l,m,n,u,v,w\}=-r}^{r} f^p_{x(l,m,n)} f^p_{x(u,v,w)} \\ &\mathbb{E}\left[\left(g_{(i-l,j-m,k-n)} - \mathbb{E}\left[g_{(i-l,j-m,k-n)}\right]\right)\left(g_{(i-u,j-v,k-w)} - \mathbb{E}\left[g_{(i-u,j-v,k-w)}\right]\right)\right]\end{aligned} \tag{15}$$

(see appendix A.1). Eq. 15 can be rewritten as

$$\sigma'^2_{x(i,j,k)} = \sum_{\{l,m,n,u,v,w\}=-r}^{r} f^p_{x(l,m,n)} f^p_{x(u,v,w)} Cov((i-l, j-m, k-n), (i-u, j-v, k-w)). \tag{16}$$

As mentioned above, we assume the covariance function to be constant over space so that the variance at a pixel becomes

$$\sigma'^2_x = \sum_{\{l,m,n,u,v,w=-r\}}^{r} f^p_{x(l,m,n)} f^p_{x(u,v,w)} Cov(l-u, m-v, n-w). \tag{17}$$

If we order the filter coefficients as a vector we can rewrite (15) as a bilinear expression using the covariance matrix Σ_{ij}:

$$\sigma'^2 = \boldsymbol{f}^{pT} \Sigma_{ij} \boldsymbol{f}^p \tag{18}$$

with $i, j = -lmn...lmn$. Since we assume isotropic noise, the expectation values of the variances $\sigma'^2_{y(i,j,k)}$ and $\sigma'^2_{z(i,j,k)}$ of $g'_{y(i,j,k)}$ and $g'_{z(i,j,k)}$ are equal so that

$$\sigma'^2_z = \sigma'^2_y = \sigma'^2_x. \tag{19}$$

Let $\sigma^2_{x^2}$ be the variance of g'^2_x. By definition we may write

$$\sigma'^2_{x^2} = \mathbb{E}[g'^4] - \mathbb{E}[g'^2]^2. \tag{20}$$

With a few algebraic steps one can show that, if g'_x is normally distributed, the variance of g'^2_x becomes

$$\sigma'^2_{x^2} = 2\sigma'^4_x. \tag{21}$$

(see appendix A.2 for more details). Finally, let σ'^2 be the variance of g'. Even though the derivatives of a random field are spatially correlated, the derivatives with respect to different spatial directions taken at the *same* point are *un*correlated in an isotropic random field. In this case, the variance of the sum in (4) is equal to the sum of the individual variances, so that

$$\sigma'^2 = 6\sigma'^4_x \tag{22}$$

Equations (22) and (17) relate the noise of the image filtered with (11) to the noise of the unfiltered image. This estimate of the noise in the resultant image $g\prime$ allows for the choice of a threshold at a given significance level.
For real images we expect to improve the signal-to-noise ratio by a similar amount as shown in fig. 10. A drawback of this method is that it enhances defects as well as edges. As a workaround, we only apply this technique to the interior region of the object, which we determine by eroding the union of object and defect region (fig. 7(b) and fig. 8). Fig. 12(b) shows the region of interest, on which we detect defects. The technique will therefore still be incapable of detecting surface defects such as the one shown in fig. 9(a).

An overview of the complete procedure is given in fig. 13. The diagram shows three main execution threads: one for calculating the signal-to-noise ratio (noise estimation), one for filtering and a third one for creating the region in which defect detection is allowed (ROI selection). Sequence diagrams of the algorithm can be found in appendix D. In the next section we will present results and discuss in detail the parameters used.

6.3.4 Results Fig. 14(b) shows the original image filtered according to (5) divided by the noise given by (22) or, in other words, the amplitude-noise-ratio (ANR). The ANR approximately has a χ^2-distribution with three degrees of freedom. Its density is given by

$$f_\chi(x) = \frac{e^{-x/2}\sqrt{x}}{2\sqrt{2}\Gamma(3/2)} \tag{23}$$

We can now select a quantile of the χ^2-distribution independent of the actual image and thus can choose a detection threshold on the ANR that is universal across samples. So instead of adjusting the threshold to the image data, we transform the image data such that the threshold can be left constant. Fig. 14(c) and (d) show the ANR binarized at thresholds 0.217 and 2.17. The parameters indicated in

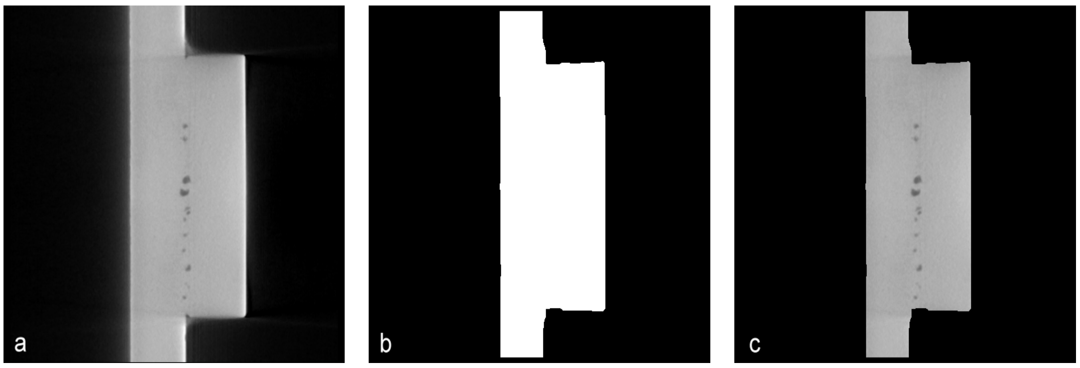

Fig. 12: Region of interest (ROI) for defect detection. (a) Original image, (b) ROI (c), ROI of original image.

fig. 13 are as follows: $Number\ of\ components = 1$ (determined by the object itself), $Size\ of\ smoothing\ kernel = 1$ (i.e. we don't smooth at all and simply apply the defect enhancement filter), $size\ of\ Erosion\ mask = 15$. The size of the smoothing kernel should be adapted to the types of defects to be detected. It should be selected such that the vector normal to the defect surface points approximately in the same direction throughout the smoothing window. A larger smoothing kernel then results in a better ANR ratio. This makes the technique especially suitable for crack detection, as these are very low in contrast, but basically planar in shape. We already took advantage of that effect when we set the kernel size to 13 in fig. 10.

Fig. 15 shows results obtained on a real crack. The kernel size has been set to 5 in this case. While increasing the kernel size can improve the detectability of planar low-contrast defects, there is a computational cost associated with a larger smoothing window, which we address in more detail when discussing performance issues in the next section. The size of the erosion mask can be chosen depending on the covariance vs. distance function in fig. 11, though we empirically set the final value to $13\sigma_{coh}$, if σ_{coh} denotes the range of the covariance function of the training data. For smaller values we obtain plenty of pseudo errors near the edges. From the fact that the value had to be chosen that large, we conclude that the statistical properties of the data near the edges are different from the interior, and additional effects contribute to the image properties at the borders as the discussion about artifacts (section 4.2.1) already suggested. The threshold values seem low, since we would expect a lot more pseudo defects at a ANR of 2.17. However bear in mind that the size of the covariance matrix equals the size of the filter vector $\boldsymbol{f}^p$ in (18). In the first example we chose $p = 0$ so we had few data to estimate the covariance matrix and poor statistical precision. Also, since the covariances of pixels close to

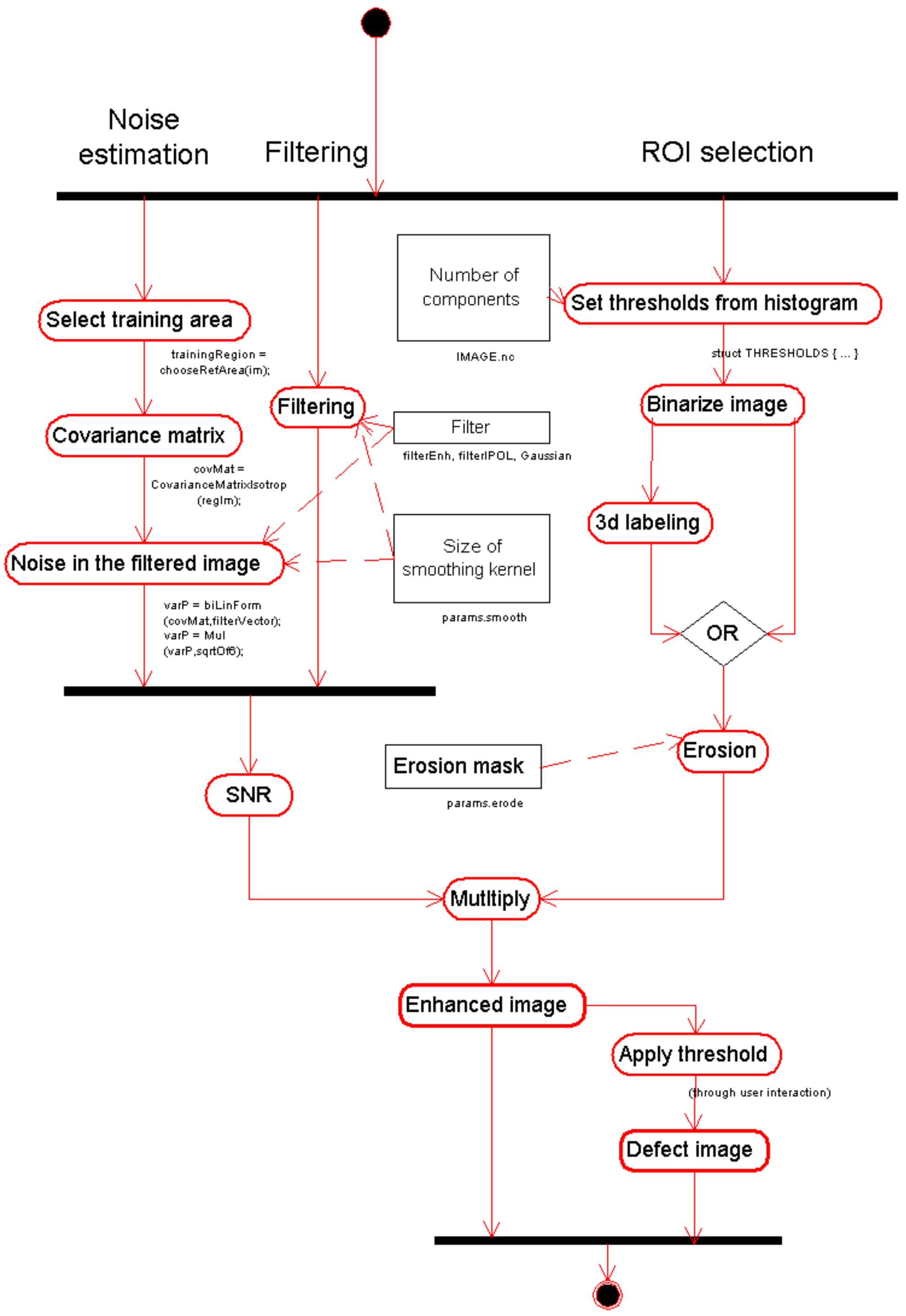
Noise estimation
Filtering
ROI selection
Select training area
trainingRegion = chooseRefArea(im);
Covariance matrix
covMat = CovarianceMatrixIsotrop (regIm);
Noise in the filtered image
varP = biLinForm (covMat,filterVector); varP = Mul (varP,sqrtOf6);
Filtering
Number of components
IMAGE.nc
Filter
filterEnh, filterIPOL, Gaussian
Size of smoothing kernel
params.smooth
Set thresholds from histogram
struct THRESHOLDS { ... }
Binarize image
3d labeling
OR
Erosion
Erosion mask
params.erode
SNR
Mutltiply
Enhanced image
Apply threshold
(through user interaction)
Defect image

Fig. 13: Overview of the complete low-contrast defect detection technique. The rectangular boxes indicate parameters supplied by the user: the number of components, the one-dimensional filter to be applied in each direction for defect enhancement, the size of the Binomial smoothing kernel (superscript p in (5)), the amount by which the image is eroded to exclude regions close to the border from defect detection, and the threshold.

each other were predominant, we actually underestimated the noise. In the case of the crack, the size of the training region was $(7 \times 7 \times 7)$ (since we used a $(5 \times 5 \times 5)$ smoothing kernel). Figures 15(c) and (d) show the SNR image at thresholds 1 and 13 respectively.

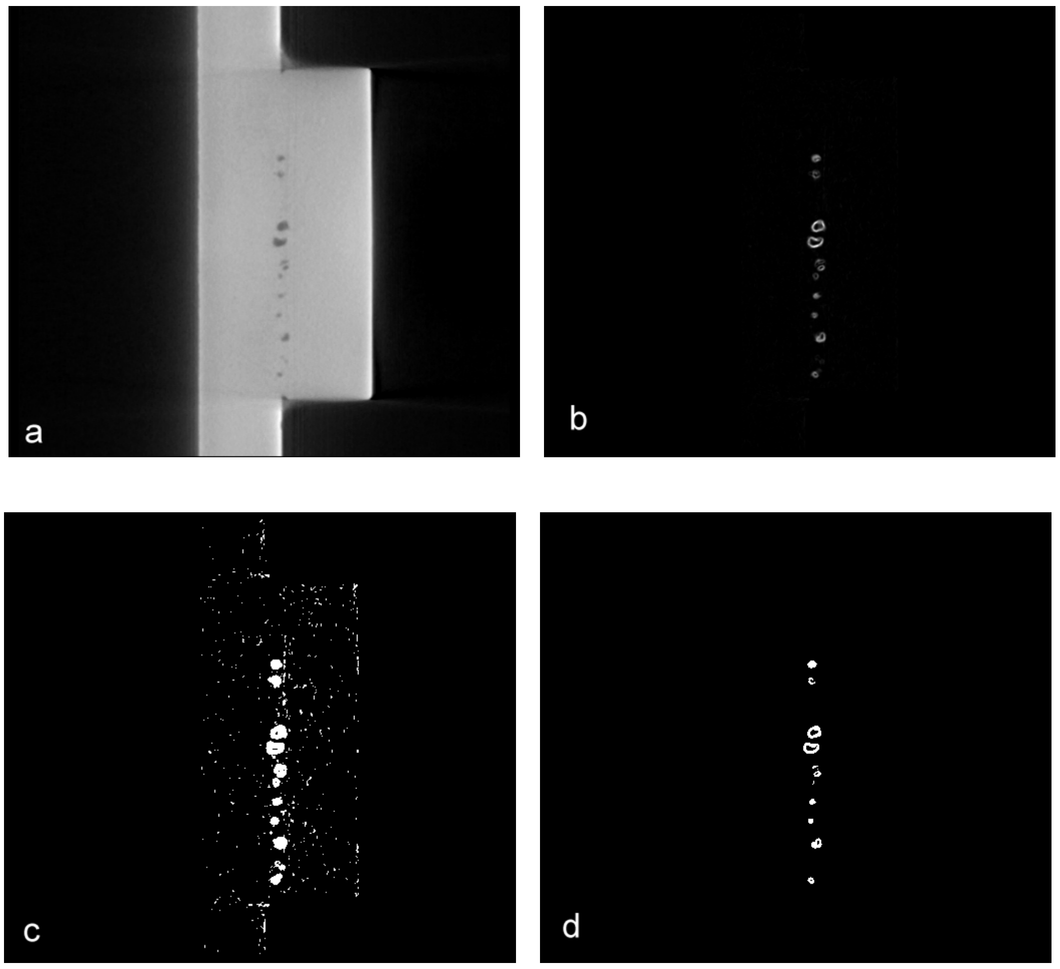

Fig. 14: Panel (b) shows the signal-to-noise ratio after (a) has been filtered with (5). (c) and (d): the image in (b) binarized at thresholds 0.217 and 2.17 respectively.

Fig. 15(b) shows that there is a slight inhomogeneity of the covariance structure throughout the image, as the false alarm rate at threshold 1 appears to be bigger in the center than near the outer edges. Again, this reflects the fact that modeling the noise as homogeneous within our sample is just an approximation. Secondly, we observe an increased false alarm rate at the lower boundary of the object, which also points to the fact that our stochastic model does not adequately describe the real image near the boundaries. The range of the coherency function in this example was

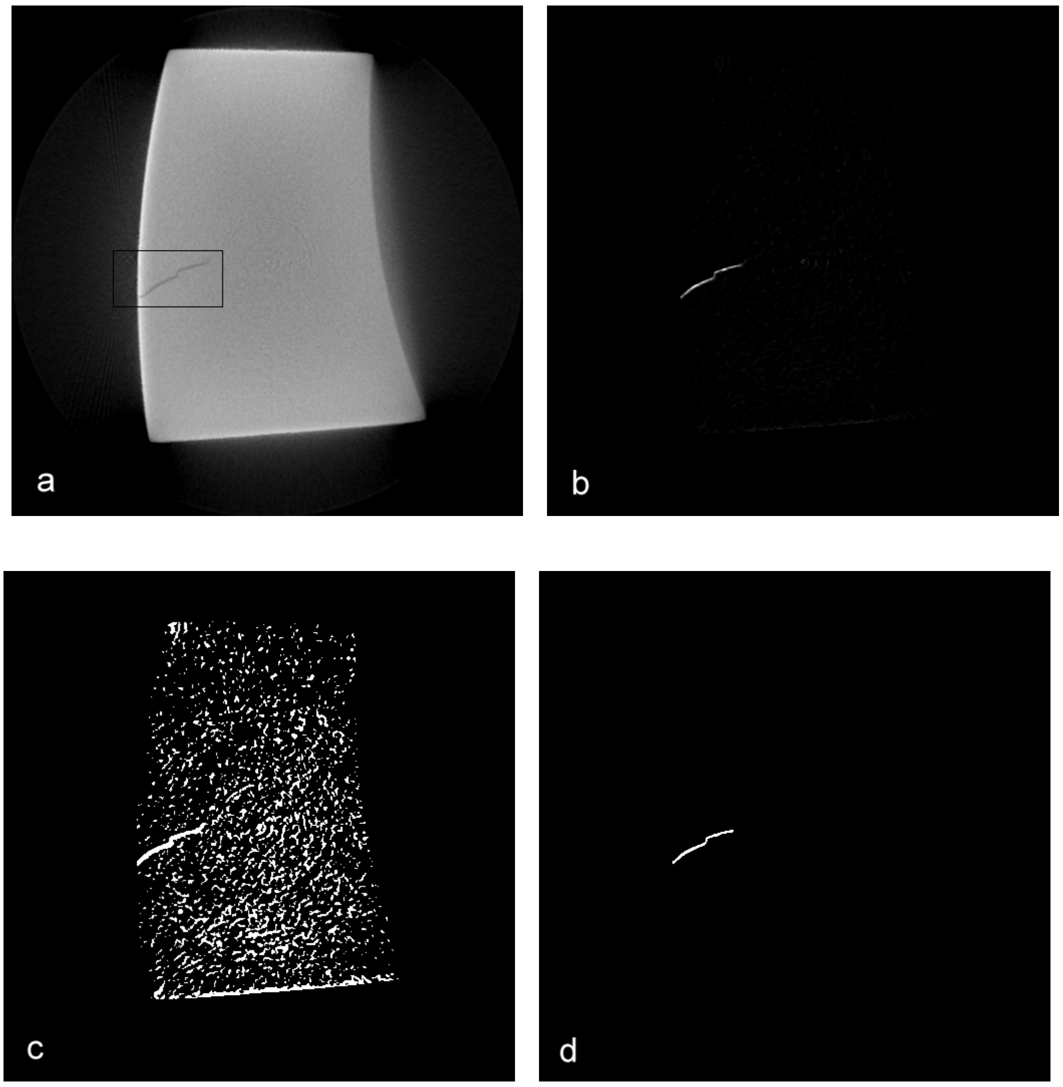

Fig. 15: (a) original image, (b) after filtering with (5), (c) binarization at 1, (d) binarization at 13.

0.83, and the size of the erosion mask was set to 5.

In contrast to the technique explained in 6.2, this method detects defect boundaries. In the next section we will fit various models to those boundaries to characterize shape and dimension of the defects with a few parameters, but first we will give some details about the algorithm's performance.

6.4 Complexity and performance

6.4.1 Complexity In this paragraph we will give a brief overview over the complexity of the computational steps involved in the algorithm. The schematic summary in fig. 13 shows three main threads of the detection algorithm:

- Noise estimation
- Filtering
- ROI selection

In the following we will estimate the number of arithmetic operations for the individual steps per voxel.

Noise estimation . Let C be the edge length of the training region. The covariance Cov_g of the grey values $g_{(l,m,n)}$, where $l, m, n = 0, ..., C-1$, is defined by

$$cov_g = \left\langle \left(g_{(l_1,m_1,n_1)} - \bar{g}\right)\left(g_{(l_2,m_2,n_2)} - \bar{g}\right)\right\rangle \tag{24}$$

Calculating the arithmetic mean $\bar{g}$ requires $\sim C^3$ additions. Calculating the covariance requires an additional $\sim 3C^6$ additions and C^6 multiplications. The covariance matrix has to be calculated only once, so the required number of additions (multiplications) per pixel is approximately $3C^6/N^3$ (C^6/N^3).

Filtering Eq. 5 gives the mathematical details of this step. Smoothing $(B_x^p B_y^p B_z^p)$ requires $3p+3$ multiplications and $3p$ additions for each term. For the derivative part ($D_{2x}S_yS_z$ etc.) 6 additions and 9 multiplications have to be performed respectively if (3×1) filters are used. This adds up to $9p+36$ multiplications and $9p+18$ additions. Summing up the squares of individual terms demands an additional 3 multiplications and 2 additions.

ROI selection The computation time of this step depends for the most part on the specific image data, so its performance will be evaluated based on concrete benchmarks in the next section.

6.4.2 Performance The performance of the algorithms has been tested on the image shown in fig. 15 (image size: $511 \times 511 \times 280$). Fig. 16 shows performance data for the three main execution threads shown in fig. 13 and discussed in the previous paragraph: noise estimation, filtering and ROI selection. The filtering is split up into the derivative ($D_{2x}S_yS_z$ etc.) and the smoothing part ($B_x^pB_y^pB_z^p$). The bottom axis corresponds to the total number of arithmetic operations (additions plus multiplications). The top axis displays the total execution time on our test data set. The vertical axis represents the size of the Gaussian smoothing filter (e.g. if the number given is 3, a (7×1) filter has been used $(3 \cdot 2 + 1 = 7)$). The time scale was chosen to match the experimental performance with the number of operations for $p = 6$. The smoothing operation accounts for the biggest part of the total execution time as the filter size is increased to achieve a better ANR (see discussion in section 6.3.4). The derivative part remains constant as the filters are not changed from those in (7). Also the parameter involved in the ROI selection has been left constant ($size\ of\ erosion\ mask = 5$). The computation time for estimating the noise is barely significant, since it does not scale with the size of the image. The next section will suggest how to optimize the smoothing procedure as it accounts for the biggest portion of the total computation time. We propose how to use more efficient filters for smoothing and will estimate the reduction in computation time upon efficient implementation.

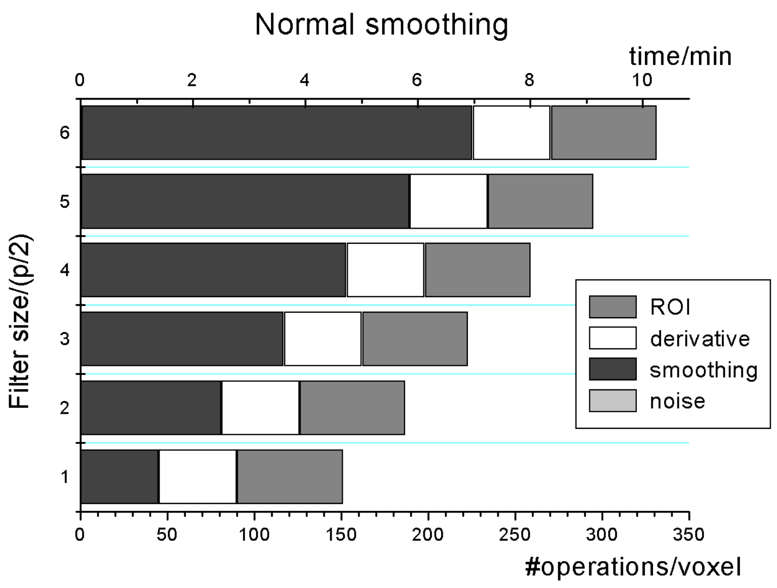

Fig. 16: Performance of the detection algorithm. The test was conducted on the image of fig. 15 with $p = 6$. The computation time for the other values of p is estimated is broken down into estimating the noise, smoothing, taking the derivatives and ROI selection.

6.4.3 Outlook: performance improvements The algorithm leaves room for performance improvements at two particular points. First the smoothing filters can be implemented more efficiently: a $(n \times 1)$ Binomial can be implemented efficiently as a network [28], reducing the number of operations from $n - 1$ additions plus n multiplications to $\sim n$ additions. Fig. 17 shows the execution time expected upon efficient implementation of the smoothing based on the reduced number of operations just mentioned. The numbers show that there will be a significant gain for larger filter sizes, and taking the derivatives and ROI selection now are the main contributors to computation time.

This concludes the work on detecting defect voxels. We will next address, how to cluster them and extract suitable parameters for shape and size description.

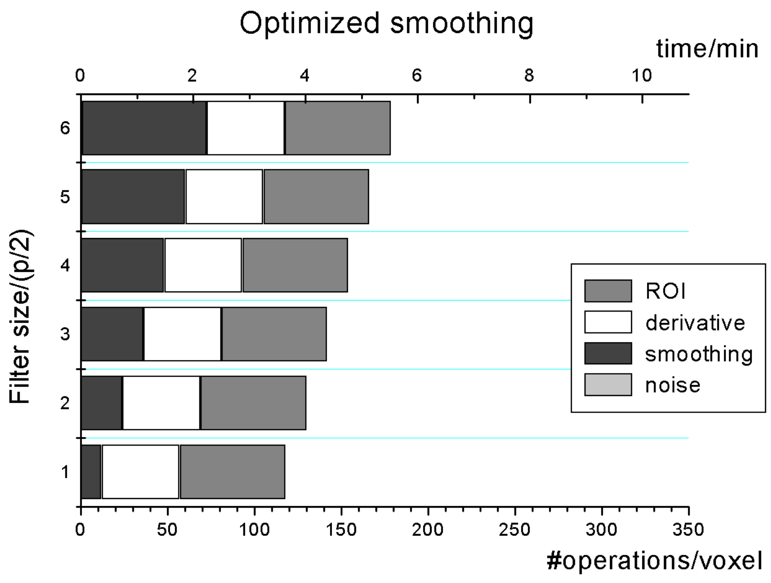

Fig. 17: Hypothetical computation time, when the Binomials are implemented efficiently as a network.

7 Feature extraction

The previous chapter has been concerned with classifying single voxels only. For quality analysis, however, features such as defect size or orientation are important. To extract those features we apply two model-based approaches. In this section we will use ellipsoids as prototypes and in the next section we will show how spherical harmonics can be used to fit models of arbitrary detail to the data. In any case, we first have to group voxels that belong to the same fault and determine its characteristics from there. Whether defects close to each other have to be counted as one is subject to specific inspection requirements for the product. In our example, defects closer than $2mm$ have to be treated as a conglomeration of defects, for which the tolerable extent is different than for individual defects. Within the scope of this work, there will be no distinction between those two types of defects, but conglomerates will be treated as such and not as single defects. A distance of $2mm$ corresponds to 4 voxels in our image. In fig. 14d we will therefore merge regions that are closer to each other than 4 voxels. This is done by performing a (5×1) morphological dilation in the x,y and z direction. The result can be observed in fig. 18. Voxels belong to the same defect if they are connected in the sense of definitions 1 and 2. To label the regions we use our 3D labeling algorithm detailed in appendix B.1.

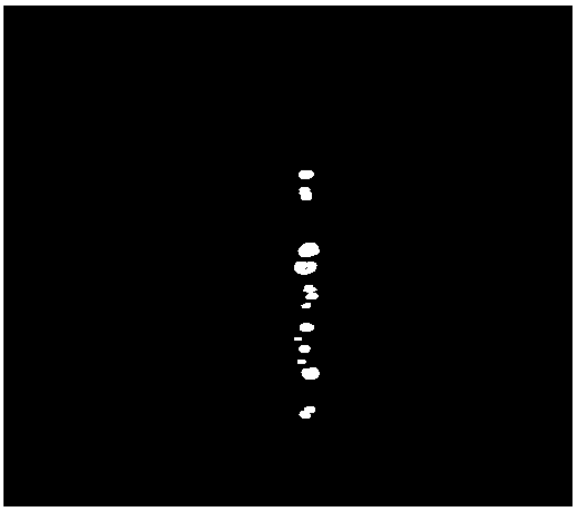

Fig. 18: Voxels belonging to the same defect are grouped together by performing a 5×1 morphological dilation on the image in fig. 14(d).

Having grouped voxels that are to be counted as one defect, we now have to extract relevant parameters such as the exact position and the maximum and minimum extent.

7.1 Ellipsoids

To extract the features of interest we first model the object boundary as an ellipsoid. This has an analogy in classical physics, namely calculating the tensor of inertia of a mass distribution. Its eigenvectors and eigenvalues yield the major and minor axes of the ellipsoid of inertia. For each region in fig. 18 we equate the grey values in the enhanced image (fig. 14(b)) with the masses and then determine the shape characteristics of the object via the 'tensor of inerta'. We first compute the 'center of mass' to obtain the defect position R for each object:

$$\boldsymbol{R} = \frac{\sum g_i \boldsymbol{r_i}}{\sum g_i} \tag{25}$$

Extending the grey value-mass analogy, we can calculate the 'tensor of inertia' for each defect:

$$J = \begin{pmatrix} J_{xx} & J_{xy} & J_{xz} \\ J_{yx} & J_{yy} & J_{yz} \\ J_{zx} & J_{zy} & J_{zz} \end{pmatrix} \tag{26}$$

J is symmetric and has the components

$$\begin{aligned} J_{xx} &= \sum (y_i^2 + z_i^2) g(\boldsymbol{x_i}) \\ J_{yy} &= \sum (x_i^2 + z_i^2) g(\boldsymbol{x_i}) \\ J_{zz} &= \sum (x_i^2 + y_i^2) g(\boldsymbol{x_i}) \\ J_{xy} &= \sum (x_i y_i) g(\boldsymbol{x_i}) \\ J_{xz} &= \sum (x_i z_i) g(\boldsymbol{x_i}) \\ J_{yz} &= \sum (y_i z_i) g(\boldsymbol{x_i}) \end{aligned} \tag{27}$$

In the coordinate system spanned by the eigenvectors of J, the normalized tensor components $J_{nn}/\sum g(\boldsymbol{x_i})$ $(n \in \{x, y, z\})$ are the expectation values of the main radii of the best-fit ellipsoid to the data. Fig. 19 recapitulates the steps to obtain those radii starting from the enhanced and defect image. The related sequence diagrams are displayed in appendix D and. Fig. 20 shows results on one of the detected defects. The data set in the left column can be well approximated by an ellipse, whereas the one in the right column exhibits significant deviations from an elliptical shape. Here a more sophisticated model is required, which will be introduced in the next section.

7.2 Spherical Harmonics

7.2.1 The mathematical model In this paragraph we provide a more general representation of three-dimensional objects that can be adapted to the level of detail required. We hereby approximate the point cloud using spherical harmonics. The

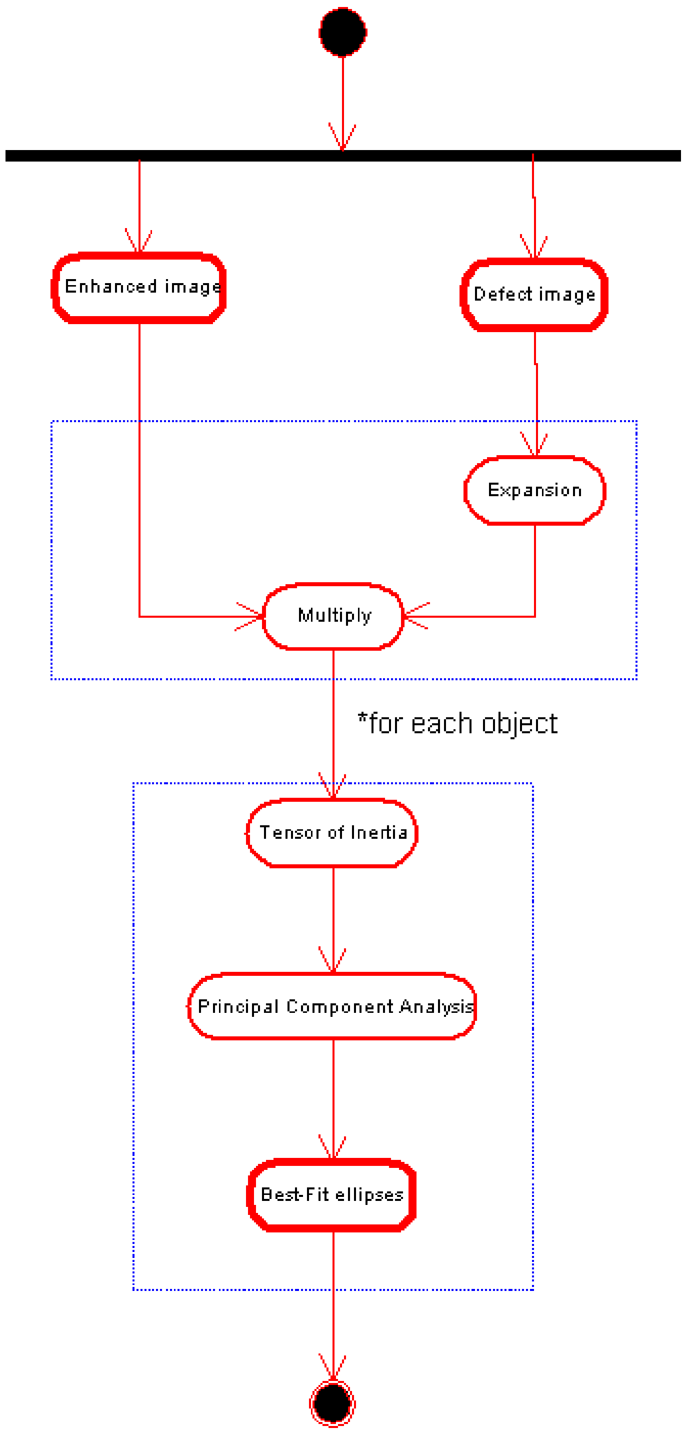

Fig. 19: Computing the principal defect axes based on the tensor of inertia.

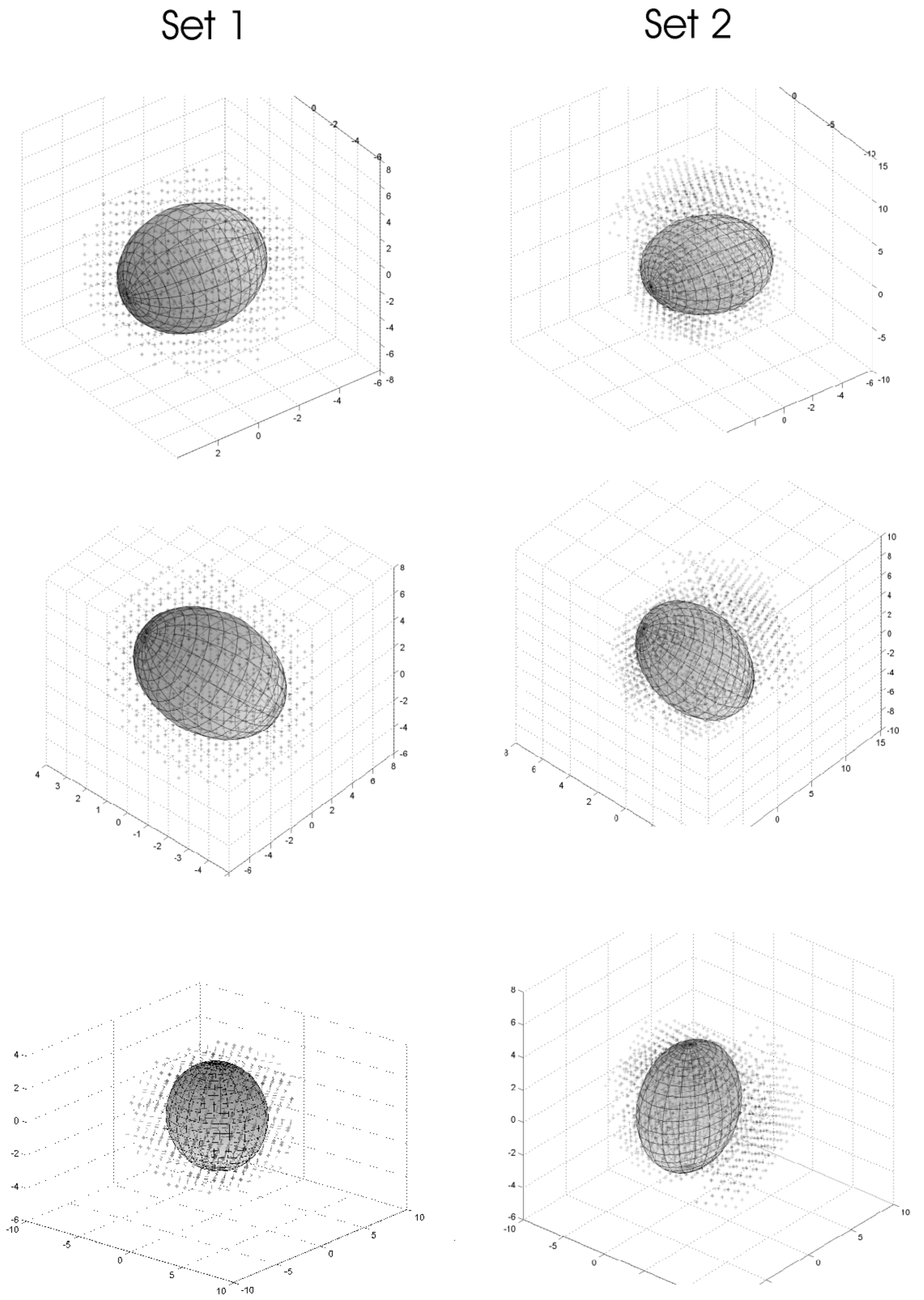

Fig. 20: Modeling a defect with an ellipse (for each column, the figures show three orthogonal views of the same plot). Left column: the ellipse fits the data pretty well. Right column: the points form a shape that deviates significantly from an ellipse.

spherical harmonics form a complete orthonormal set of functions in $L_2(S_1)$ where S_1 represents the unit sphere. In R_3 they are defined as

$$Y_l^m(\theta,\phi) = {Y_l^m}_e(\theta,\phi)+{Y_l^m}_o(\theta,\phi) = P_l^m(cos\theta)\left(cos(m\phi)+sin(m\phi)\right), m=0,1,2,...,l \tag{28}$$

where P_l^m are the associated legendre polynomials. A linear combination of the Y_l^m can describe arbitrarily complex objects $R(\theta,\phi)$ in spherical coordinates:

$$R(\theta,\phi) = \sum_{m,l} a_l^m {Y_l^m}_e(\theta,\phi) + b_l^m {Y_l^m}_o(\theta,\phi) \tag{29}$$

The odd functions ${Y_l^m}_o$ all change sign under the transformation $\phi \rightarrow -\phi$ and exhibit a shape rather untypical for defects. We hence use the even part only, so our approximation becomes

$$R(\theta,\phi) = \sum_{m,l} a_l^m P_l^m(cos\theta)cos(m\phi) \tag{30}$$

where the sum can be truncated according to the level of shape detail one is interested in. Fig. 21 shows the even part of a few of the basis functions. The next section addresses how to estimate the coefficients in (30) based on the real data.

7.2.2 Adaption to real data

Saupe et al. used spherical harmonics to extract features from 3D models that could be used to retrieve similar objects from a database [16]. They estimated the coefficients of the expansion via a spherical FFT algorithm. We will take a different approach, i.e. we will use a least squares estimator to fit each model to our data. Given a set of points in spherical coordinates $(r_i,\theta_i,\phi_i,g_i)$, where g_i denotes the grey value, we need to find the coefficients in (30) such that

$$S := \sum_i g_i^2 \left(r_i - \sum_{m,l} a_l^m {Y_l^m}_e(\theta_i,\phi_i)\right)^2 \longrightarrow min. \tag{31}$$

The sum represents the average radius as a function of (θ,ϕ). Eq. 31 requires

$$\frac{\partial S}{\partial a_l^m} = 0 \tag{32}$$

for all a_l^m to be considered. Equation 32 is a system of linear equations which can be expressed as:

$$G \cdot \boldsymbol{a} = \boldsymbol{d} \tag{33}$$

If we truncate the sum in (32) after n terms, G is an $n \times n$ matrix with the entries

$$G_{lm} = \sum_{i=1}^{N} g_i^2 f_l(\theta_i,\phi_i) f_m(\theta_i,\phi_i) \tag{34}$$

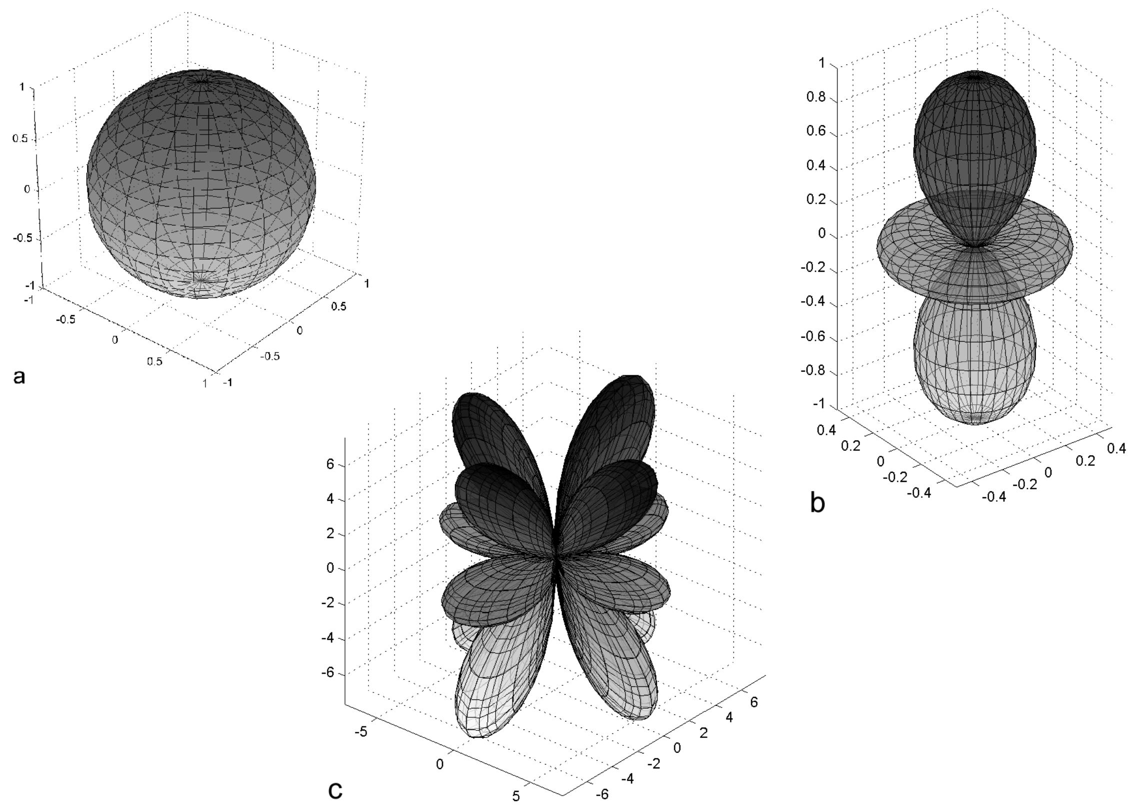

Fig. 21: A few representatives of even spherical harmonics: (a) $Y_{0\ e}^{0}$. (b) $Y_{2\ e}^{0}$. (c) $Y_{4\ e}^{2}$

and d is an $(n \times 1)$ vector with components

$$d_n = \sum_{i=1}^{N} g_i^2 f_n(\theta_i, \phi_i) r_i \tag{35}$$

Here we replaced the Y_l^m with f_n, so that

$$f_0 = Y_{0\ e}^{0}, \quad f_1 = Y_{1\ e}^{0}, \quad f_2 = Y_{1\ e}^{1}, \quad f_3 = Y_{2\ e}^{0} \tag{36}$$

and so on. To solve for the coefficients, we invert the matrix G via singular value decomposition.

7.2.3 Results Figs. 22 through 24 show the results obtained on the data set shown in the second column of fig. D at various orders. In case of the second order, for example, the number of free parameters is 6: a_0^0,a_1^0,a_1^1,a_2^0,a_2^1,a_2^2. The higher the order the more shape details are resolved. Since we weighted the fit with the grey value (see eq. 31) the surface tends to follow the dark points more closely and ignore the lighter ones. Again, sequence diagrams can be found in the appendix.

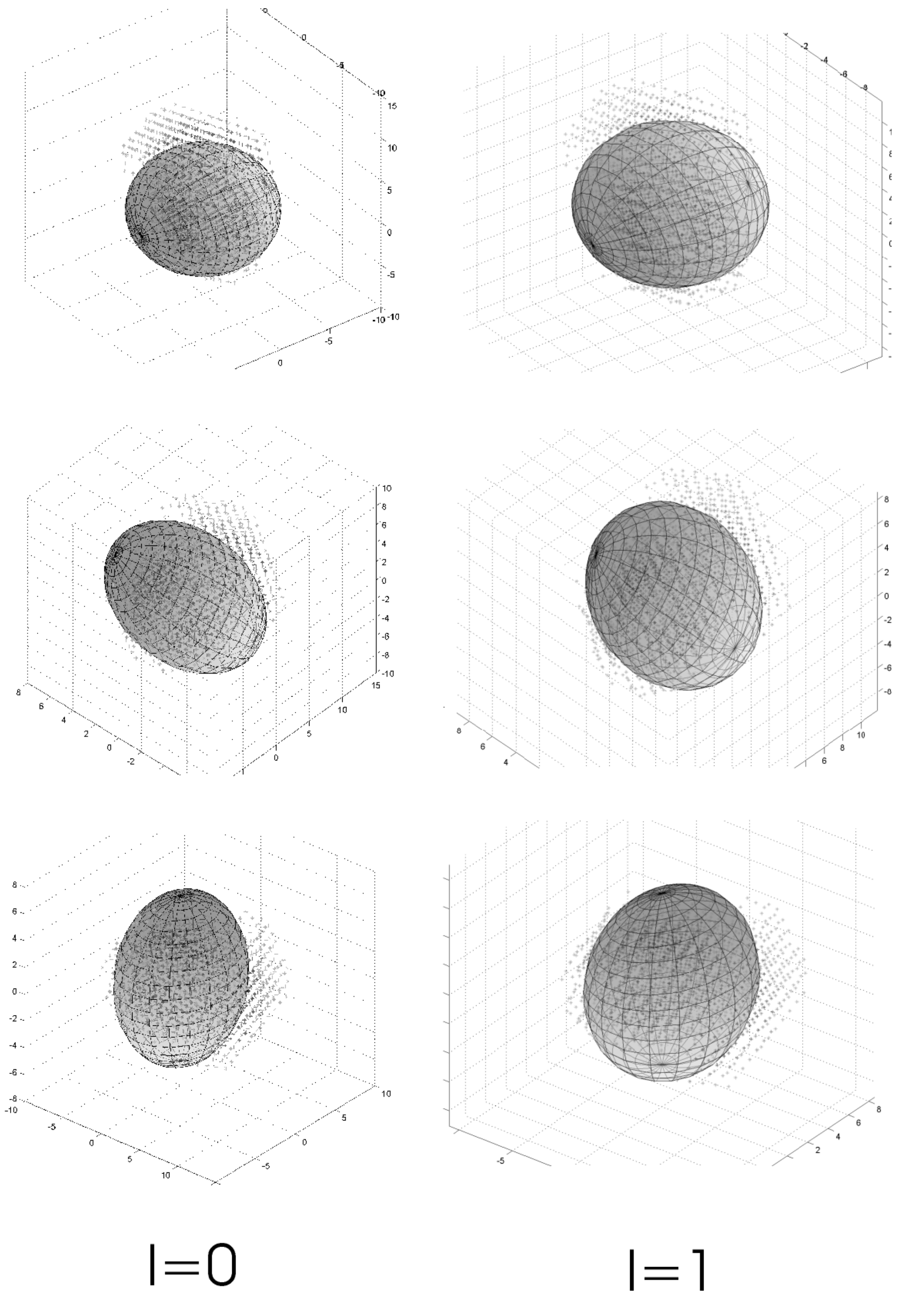

Fig. 22: Zero and first order fit.

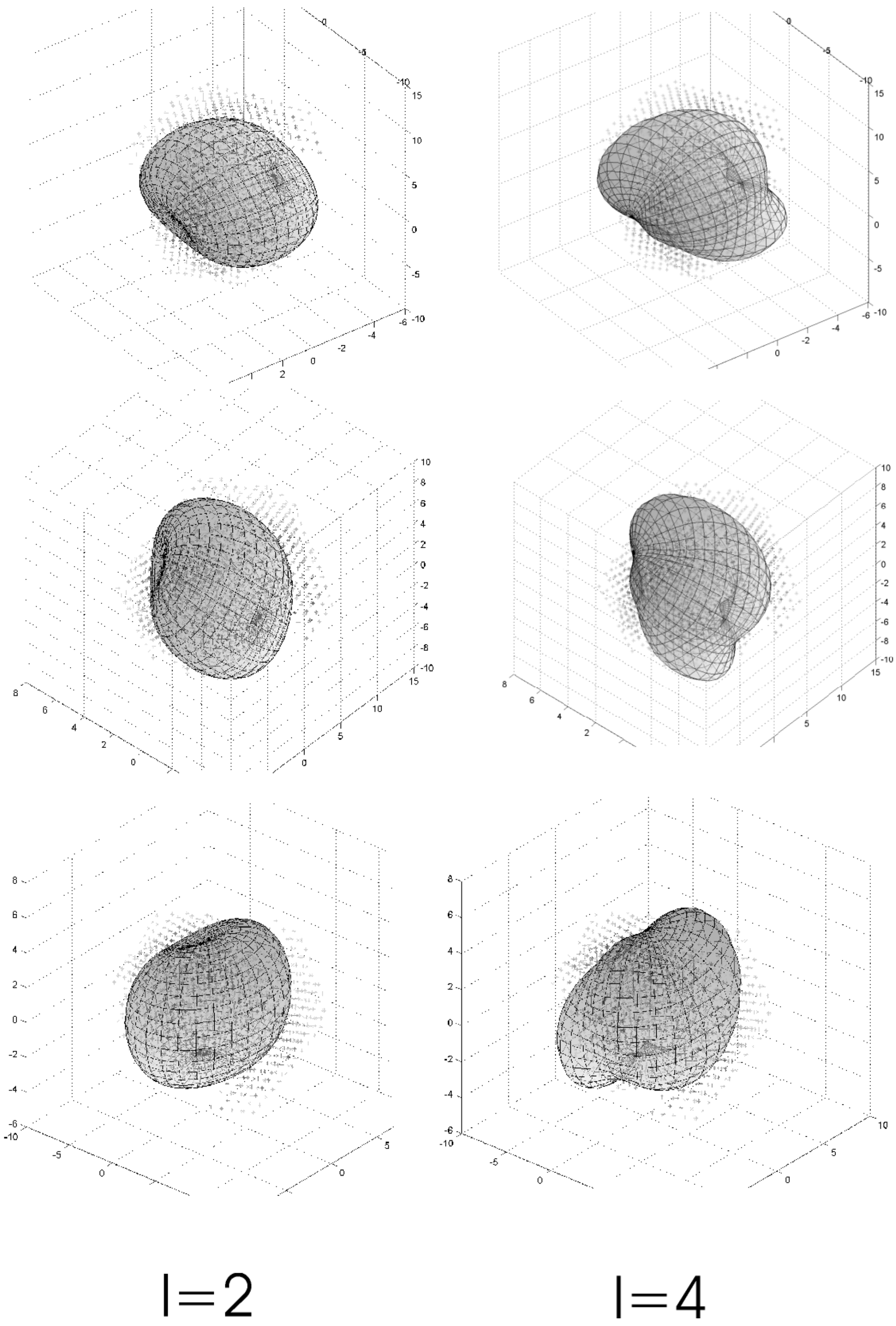

Fig. 23: Second and fourth order fit.

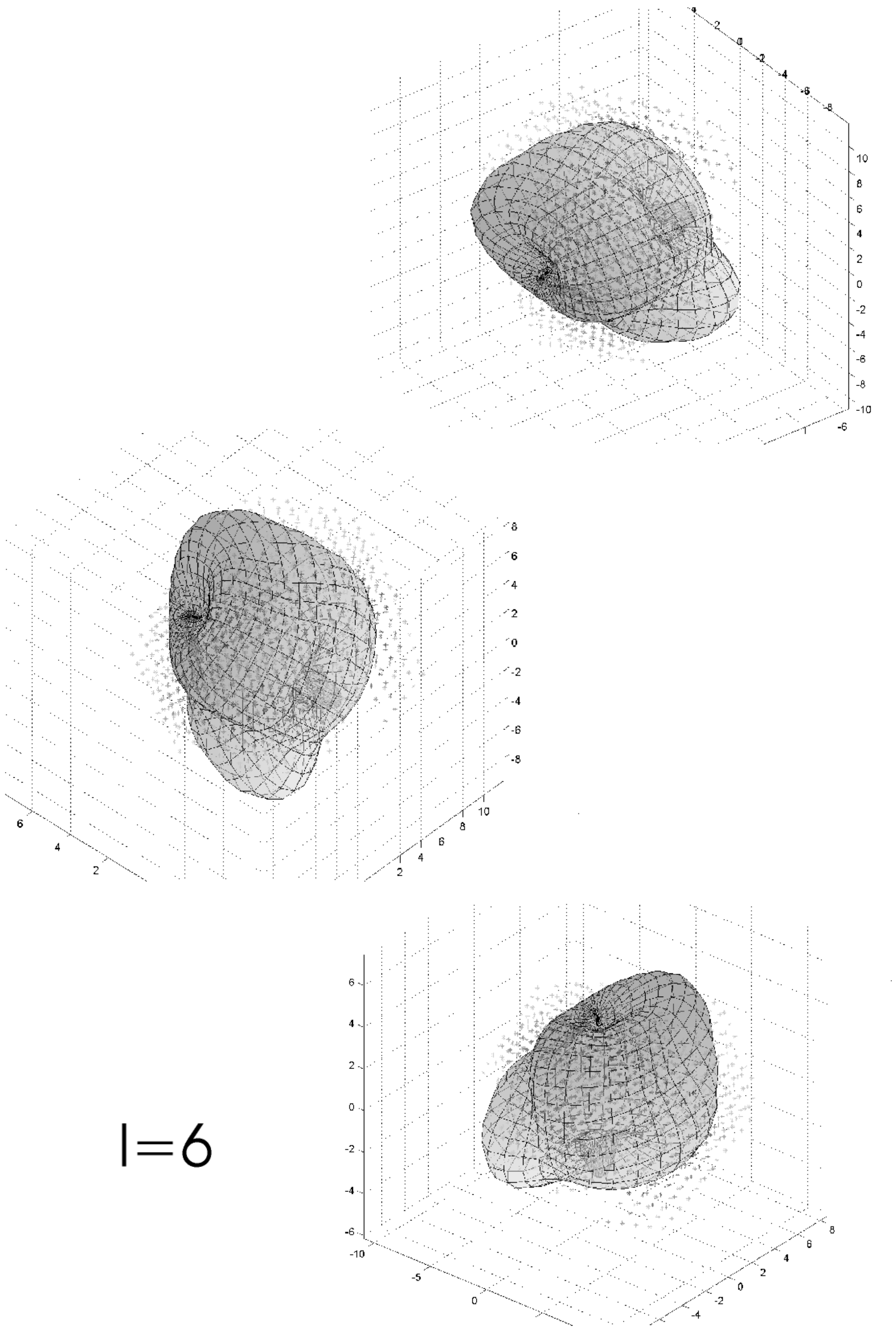

Fig. 24: Sixth order fit.

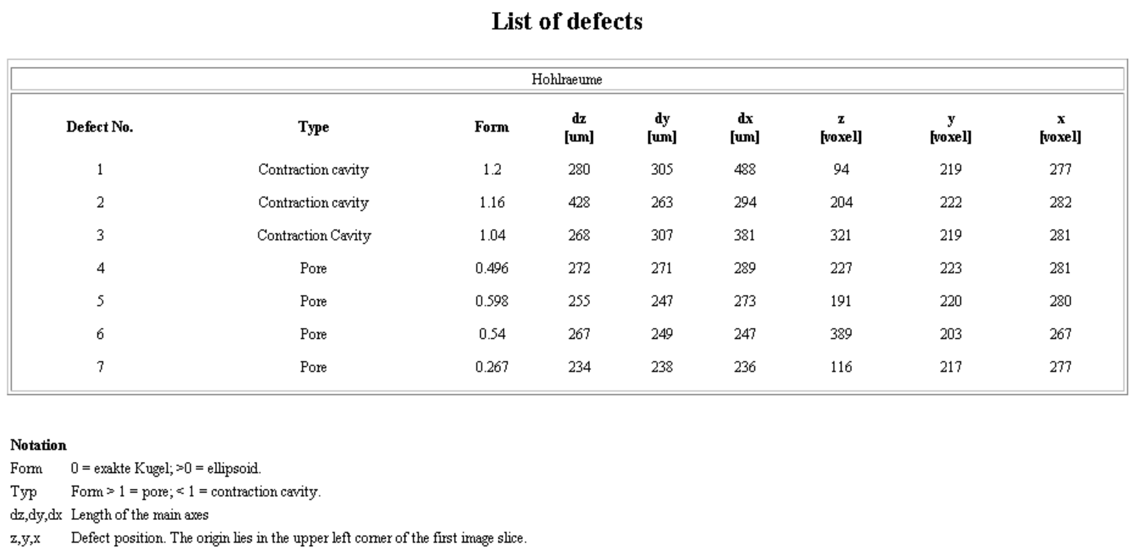

List of defects

Hohlraeume								
Defect No.	**Type**	**Form**	**dz [um]**	**dy [um]**	**dx [um]**	**z [voxel]**	**y [voxel]**	**x [voxel]**
1	Contraction cavity	1.2	280	305	488	94	219	277
2	Contraction cavity	1.16	428	263	294	204	222	282
3	Contraction Cavity	1.04	268	307	381	321	219	281
4	Pore	0.496	272	271	289	227	223	281
5	Pore	0.598	255	247	273	191	220	280
6	Pore	0.54	267	249	247	389	203	267
7	Pore	0.267	234	238	236	116	217	277

Notation

Form	0 = exakte Kugel; >0 = ellipsoid.
Typ	Form > 1 = pore; < 1 = contraction cavity.
dz,dy,dx	Length of the main axes
z,y,x	Defect position. The origin lies in the upper left corner of the first image slice.

Fig. 25: Defect protocol

8 From the raw data to the inspection protocol

The objective of image processing techniques in industrial quality control is to generate a data protocol, that allows for direct comparison of measured defects with inspection requirements. The algorithms we introduced in this paper can be used to generate necessary data such as the location of defects, their extent and shape characteristics.

Fig. 25 shows such a protocol obtained with the methods detailed in section 6 and 7. The 'List of defects' displays defect postions and features. This list has been generated fully automatically from a raw data set after entering just a few parameters as indicated in fig. 13. Appendix C will give some details about the software that we have designed to automate this task.

9 Conclusion and outlook

This work contains techniques for the automated defect detection and feature extraction in X-ray CT images. The methods are universal and applicable to a wide range of data. They mark one of the first attempts to bring 3D image processing techniques to the field of industrial inspection. We managed to keep the processing time below the amount required for recording and reconstruction, which makes the algorithms useful for integration into a real system. Appendix C details aspects of the GUI based software application developed within the scope of this work that automatically generates a fault protocol after processing the raw data supplied by the user.
This thesis marks a first step towards automating a CT inspection system. Future work includes the application of our algorithms and software packages towards concrete inspection tasks. To fully automate the detection process described in section 6.3 the statistical analysis can be refined by estimating the covariance structure of the noise locally and robustly and by using a more general random field model. Also it is desirable to find an objective threshold on the ANR.

Appendix

A Calculations and proofs

A.1 Error propagation

Step from (14) to (15): Substituting (13) in (14) yields

$$\begin{aligned}\sigma'^2_{x(i,j,k)} = \mathbb{E}\Bigg[\sum_{l,m,n} f^p_{(l,m,n)} g_{(i-l,j-m,k-n)} - \mathbb{E}\left[\sum_{l,m,n} f^p_{(l,m,n)} g_{(i-l,j-m,k-n)}\right] \\ \sum_{u,v,w} f^p_{(u,v,w)} g_{(i-u,j-v,k-w)} - \mathbb{E}\left[\sum_{u,v,w} f^p_{(u,v,w)} g_{(i-u,j-v,k-w)}\right]\Bigg]\end{aligned} \tag{37}$$

The expectation value of a finite sum of random variables equals the sum of their expectation values. We may therefore rewrite (37) as

$$\begin{aligned}\sigma'^2_{x(i,j,k)} = \sum_{\{l,m,n,u,v,w\}=-r}^{r} f^p_{x(l,m,n)} f^p_{x(u,v,w)} \\ \mathbb{E}\left[\left(g_{(i-l,j-m,k-n)} - \mathbb{E}\left[g_{(i-l,j-m,k-n)}\right]\right)\left(g_{(i-u,j-v,k-w)} - \mathbb{E}\left[g_{(i-u,j-v,k-w)}\right]\right)\right]\end{aligned} \tag{38}$$

A.2 The variance of a squared gaussian random variable

This paragraph derives the relation between the variances of a Gaussian random variable and its square. Let y be a normally distributed random variable with variance σ_y^2 and probability density

$$f(y) = \frac{1}{\sigma\sqrt{2\pi}} e^{-\frac{y^2}{2\sigma_y^2}}. \tag{39}$$

The variances of y and y^2 are by definition

$$\begin{aligned} \sigma_y^2 &= \mathbb{E}\left[y^2\right] - \mathbb{E}\left[y\right]^2 \\ \sigma_{y^2}^2 &= \mathbb{E}\left[y^4\right] - \mathbb{E}\left[y^2\right]^2 \end{aligned} \tag{40}$$

The expectation value of y is zero, so (40) becomes

$$\sigma_{y^2}^2 = E\left[y^4\right] - \sigma_y^4 \tag{41}$$

On the other hand, the expectation value of y^4 is

$$\mathbb{E}\left[y^4\right] = \int_{-\infty}^{\infty} y^4 e^{-\frac{y^2}{2\sigma^2}dy}. \tag{42}$$

Using

$$\int_0^{\infty} x^n e^{-ax^2} = \frac{\Gamma\left(\frac{n+1}{2}\right)}{2a^{\left(\frac{n+1}{2}\right)}} \tag{43}$$

we obtain

$$\mathbb{E}\left[y^4\right] = \frac{4\Gamma\left(\frac{5}{2}\right)}{\sqrt{\pi}}\sigma_y^4 = 3\sigma_y^4. \tag{44}$$

Substituting (44) in (41) finally yields

$$\sigma_{y^2}^2 = 2\sigma_y^4 \tag{45}$$

B Algorithmic details

B.1 3D labeling

The algorithm for labeling separated regions in the image is implemented in two steps: First mark all background pixels of the binarized image transparent and all object pixels opaque. Then consider a parallel beam light source illuminating one side of the object (see fig. 27(a)) and mark all voxels struck by any of the light rays as illuminated. Repeat this procedures for the other 5 sides of the object. After that, create a list of the coordinates of all remaining 'shaded' points that are neighbors of 'illuminated' points. Then mark those voxels as illuminated and repeat the previous step. Iterate this procedure until no more voxels are converted. Fig. 26 gives a schematic summary of the algorithm. The final result can be observed in fig. 27(c).

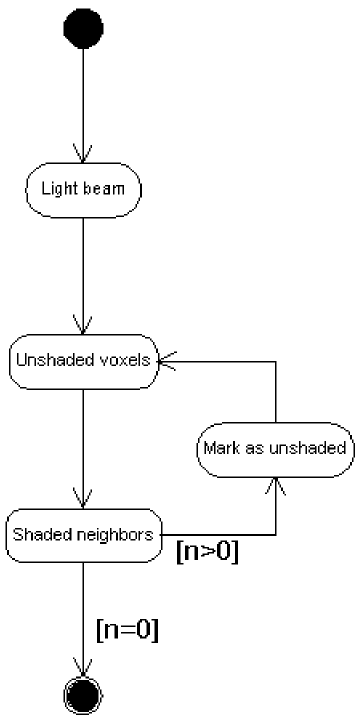

Fig. 26: Schematic summary of the 3D labeling algorithm

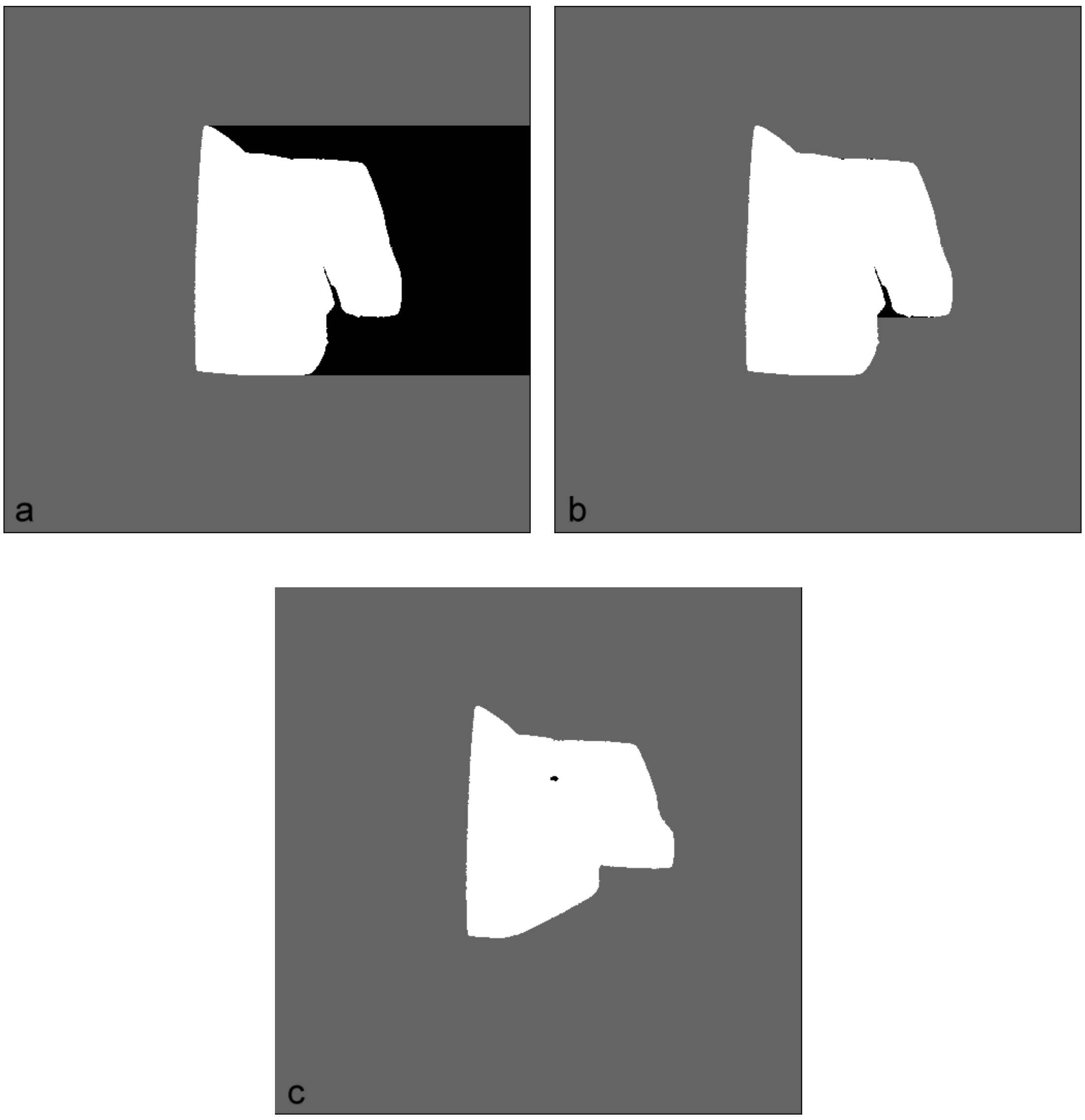

Fig. 27: Steps of the 3D labeling algorithm: (a) 'Illuminating' from one side (b) two sides and (c) final result.

C Software architecture

Besides providing basic image processing algorithms, the objective of the project was to build a user-friendly software application to visualize, store and retrieve processing results. Fig. 28 shows a screenshot of the application running under Windows with various controls for interactive visualization and data handling.

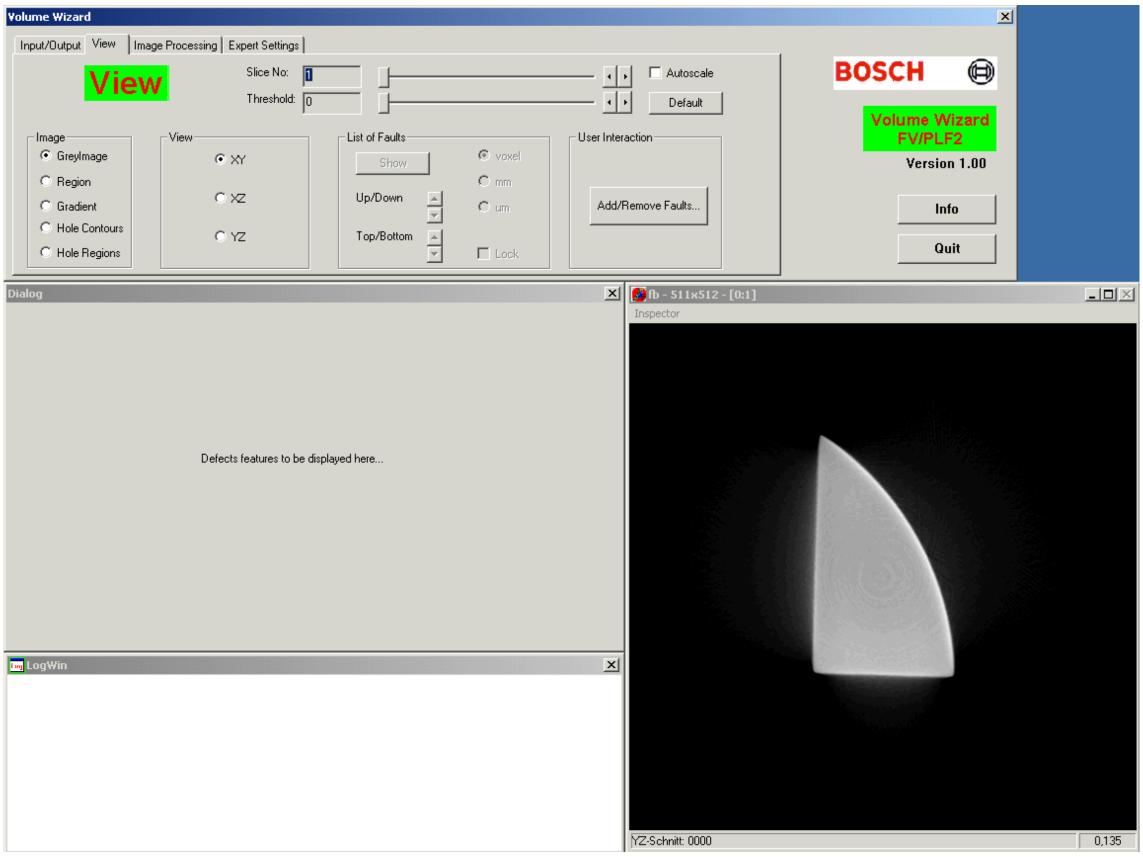

Fig. 28: The user interface

C.1 Technical realization

Fig. 29 shows an overview of the architecture. We used the commercially available software package 'heurisko' to implement the image processing algorithms. Heurisko operates through an interpreted script language. Script files can be loaded and executed through an external interface. Our GUI based software uses that interface for execution control and data exchange. Fig. 30 shows some its classes: the object data retrieval is handled through the class 'hQueryInterface' and the data are stored in container classes that support ordered lists. The key handlers for start-

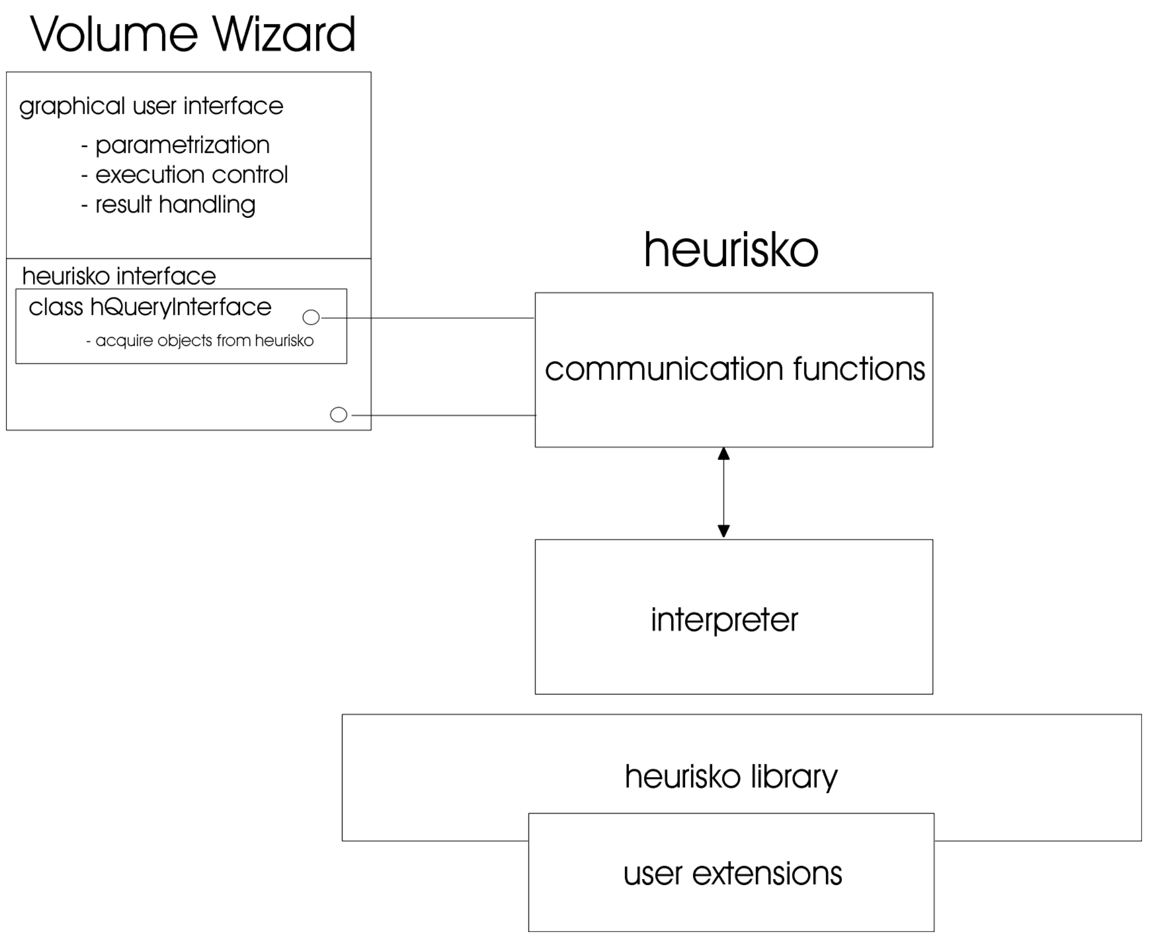

Fig. 29: Software architecture

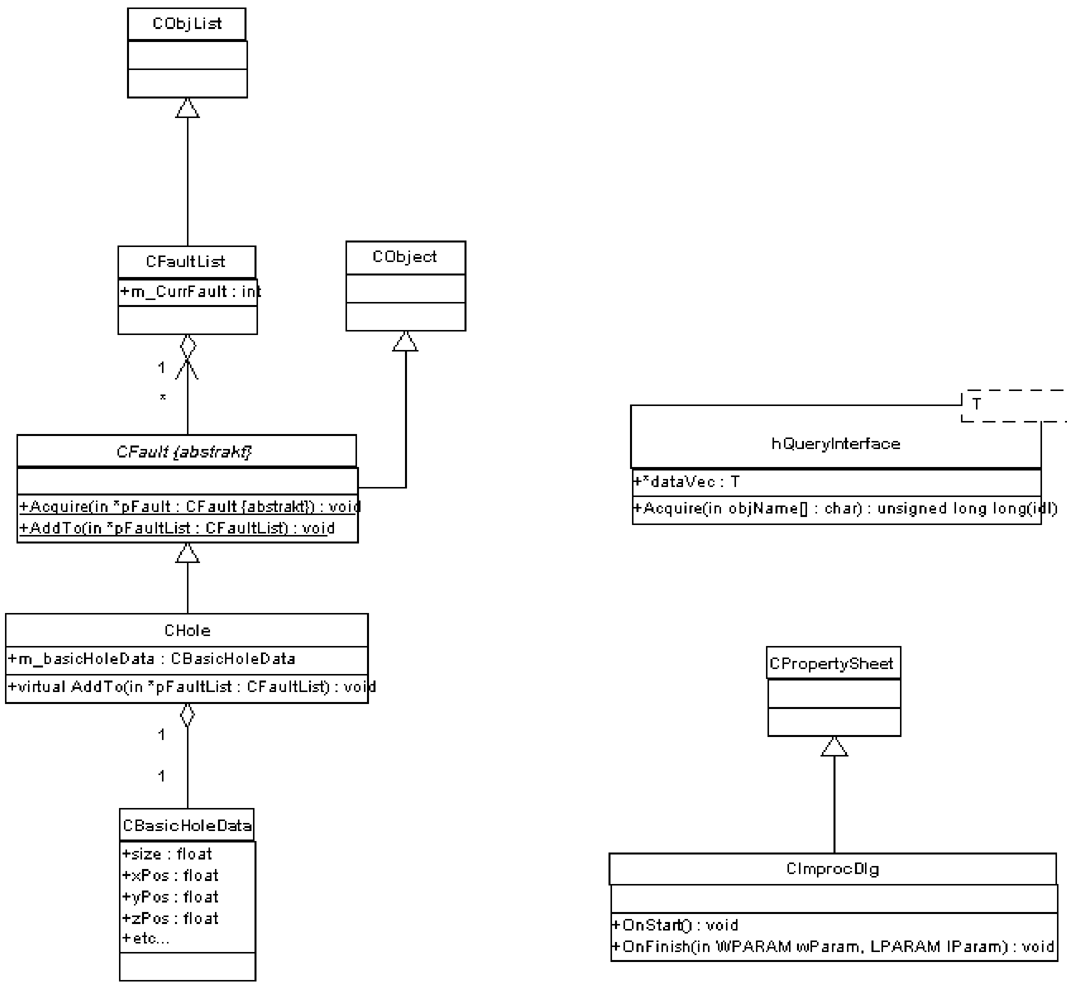
CObjList
CFaultList
+m_CurrFault : int
CObject
1
*
CFault {abstrakt}
+Acquire(in *pFault : CFault {abstrakt}) : void
+AddTo(in *pFaultList : CFaultList) : void
CHole
+m_basicHoleData : CBasicHoleData
+virtual AddTo(in *pFaultList : CFaultList) : void
1
1
CBasicHoleData
+size : float
+xPos : float
+yPos : float
+zPos : float
+etc...
T
hQueryInterface
+*dataVec : T
+Acquire(in objName[] : char) : unsigned long long(idl)
CPropertySheet
CImprocDlg
+OnStart() : void
+OnFinish(in WPARAM wParam, LPARAM lParam) : void

Fig. 30: Some of the key classes of our software application

ing the image processing and retrieving the data are 'CImprocDlg::OnStart()' and 'CImProcDlg:OnFinish()', both of which are listed below.

```
void CImProcDlg::OnStart()
{
        // TRACE("Entering hQueryInterface<T>::OnStart()\n");
        // LogwinPutStr("",1,FALSE,"%s","Entering hQueryInterface<T>::OnStart()");

        UpdateData(TRUE);

        CMainSheet* pMSheet = (CMainSheet*)GetParent();
        CFaultList* pFaultList = &pMSheet->m_faultDoc.m_faultList;
        pFaultList->RemoveAll();

        DWORD nThreadID = theApp.m_nThreadID;
        char command[1024];

        if (IsDlgButtonChecked(IDC_CHECKHOLE)) {
                ((CFaultList*)pFaultList)->Shrink("Hole");

                m_busyDlg.Create(IDD_BUSYDIALOG);
                if (m_Method == 0) {
                        sprintf(command,"HOLES(%dl)",nThreadID);
                        hCommand(command);
                }
                else {
                        sprintf(command,"go(%dl)",nThreadID);
                        hCommand(command);

                }
        }
}

void CImProcDlg::OnFinish(WPARAM wParam, LPARAM lParam) {

        CMainSheet* pMSheet = (CMainSheet*)GetParent();
        CFaultList* pFaultList = &pMSheet->m_faultDoc.m_faultList;

        ...
```

```
hQueryInterface<HOLE> hI;
hQueryInterface<IMAGE> hIMAGE;
CHole hole;
CImage image;
IMAGE Im;

...

try {
        nHoles = hI.Acquire("HOLE");
        hIMAGE.Acquire("IMAGE");
        image = hIMAGE.dataVec[0];
        ...
        throw nHoles;
}

catch (ULONG nHoles) {
        if (NONZERO(nHoles))
        {
                hQueryInterface<IMAGE> hQ;
                hQ.Acquire("IMAGE");
                Im = *hQ.dataVec;
                pMSheet->m_pImObj->Im = Im;

                CHole::counter = 0;

                for (i = 0; i < (int)nHoles; i++) {
                        hole = hI.dataVec[i];
                        hole.AddTo(pFaultList);
                        CHole::counter++;
                }
                nHoles = hI.Acquire("HOLE");
                ...
        else
        {
                AfxMessageBox("Es wurden keine Fehler gefunden!");
        }
}
...
```

D Flowchart summary

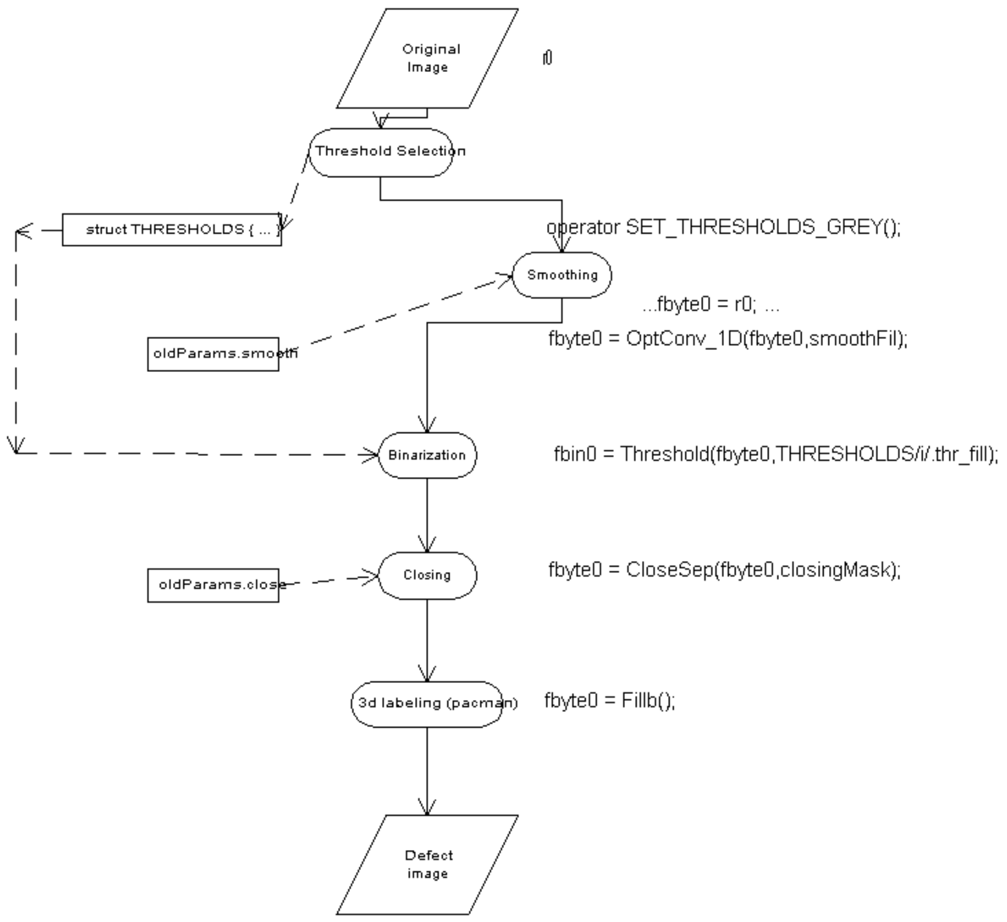
Original Image
r0
Threshold Selection
struct THRESHOLDS { ... }
operator SET_THRESHOLDS_GREY();
Smoothing
oldParams.smooth
...fbyte0 = r0; ...
fbyte0 = OptConv_1D(fbyte0,smoothFil);
Binarization
fbin0 = Threshold(fbyte0,THRESHOLDS/i/.thr_fill);
oldParams.close
Closing
fbyte0 = CloseSep(fbyte0,closingMask);
3d labeling (pacman)
fbyte0 = Fillb();
Defect image

Fig. 31: Detection algorithm with global thresholding and 3D labeling as described in section 6.1 and 6.2. The rounded boxes represent the various subroutines of the processing sequence, the rectangular boxes contain the parameters relevant for the each step, and the right column shows the respective procedure call.

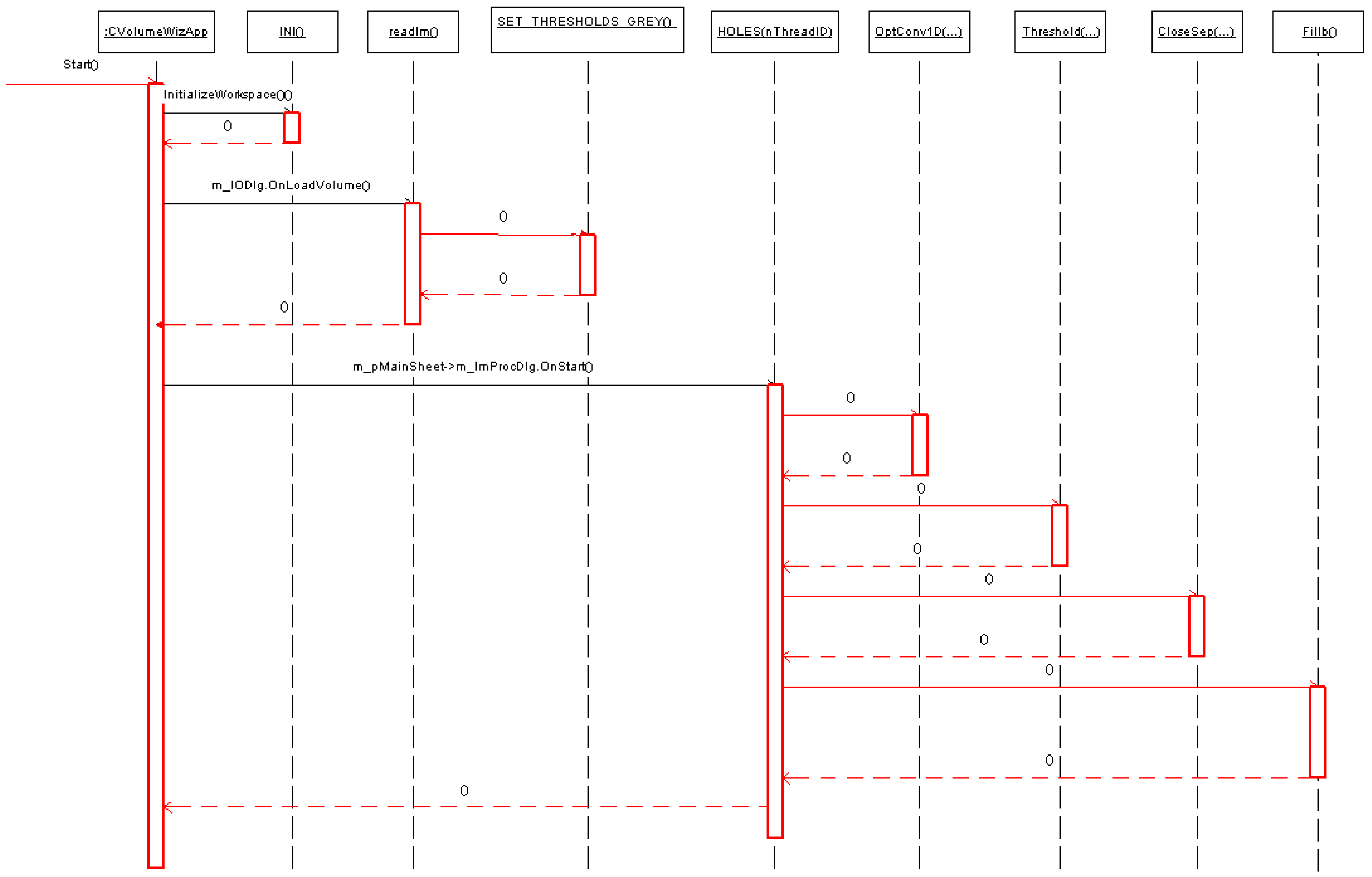

Fig. 32: The detection algorithm of section 6.1 and 6.2 as a sequence diagram.

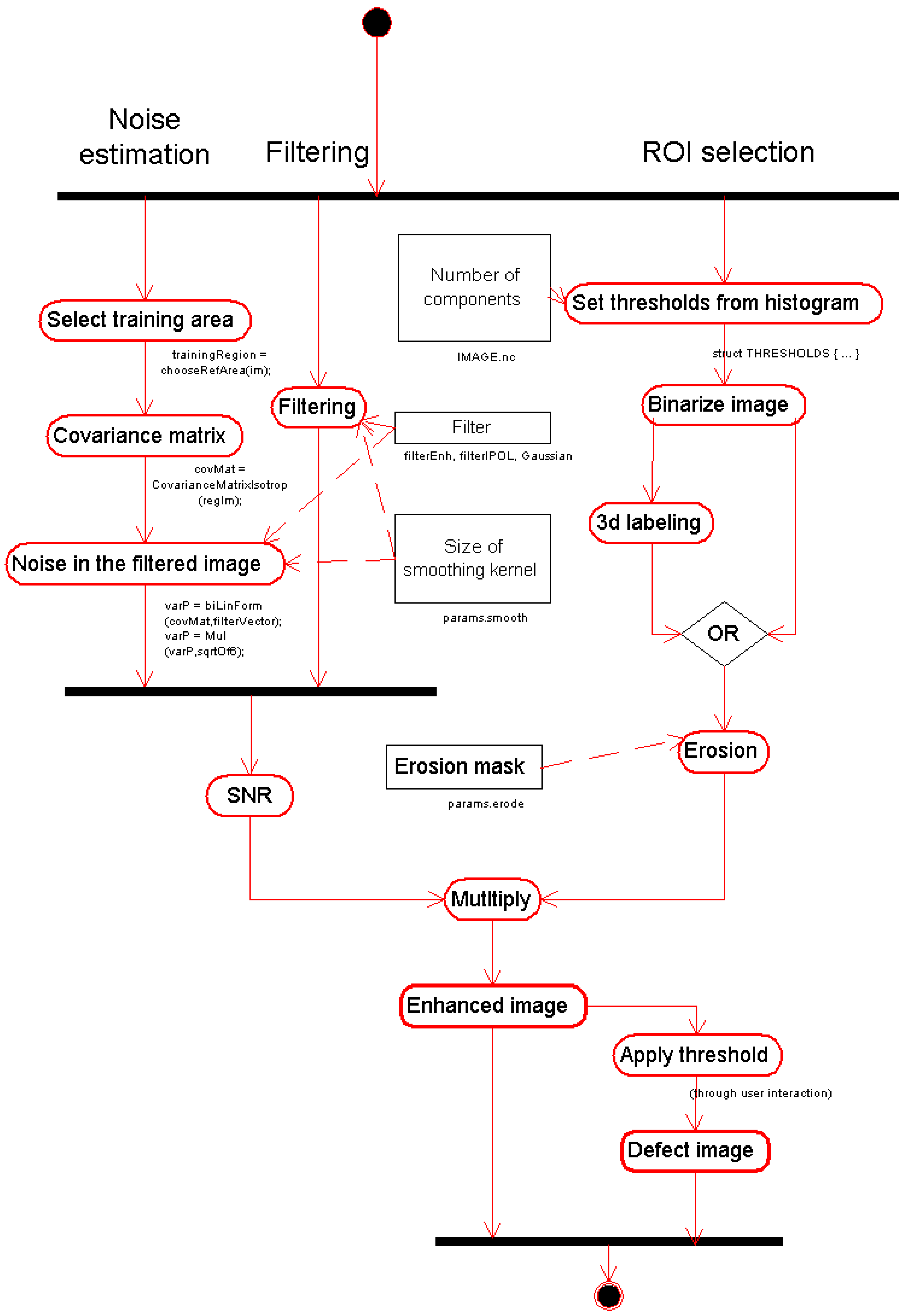
Noise estimation
Filtering
ROI selection
Select training area
trainingRegion = chooseRefArea(im);
Covariance matrix
covMat = CovarianceMatrixIsotrop (regIm);
Noise in the filtered image
varP = biLinForm (covMat,filterVector); varP = Mul (varP,sqrtOf6);
Filtering
Number of components
IMAGE.nc
Filter
filterEnh, filterIPOL, Gaussian
Size of smoothing kernel
params.smooth
Set thresholds from histogram
struct THRESHOLDS { ... }
Binarize image
3d labeling
OR
Erosion
Erosion mask
params.erode
SNR
Mutltiply
Enhanced image
Apply threshold
(through user interaction)
Defect image

Fig. 33: The activity diagram for the routine described in section 6.3 with associated objects and procedure calls.

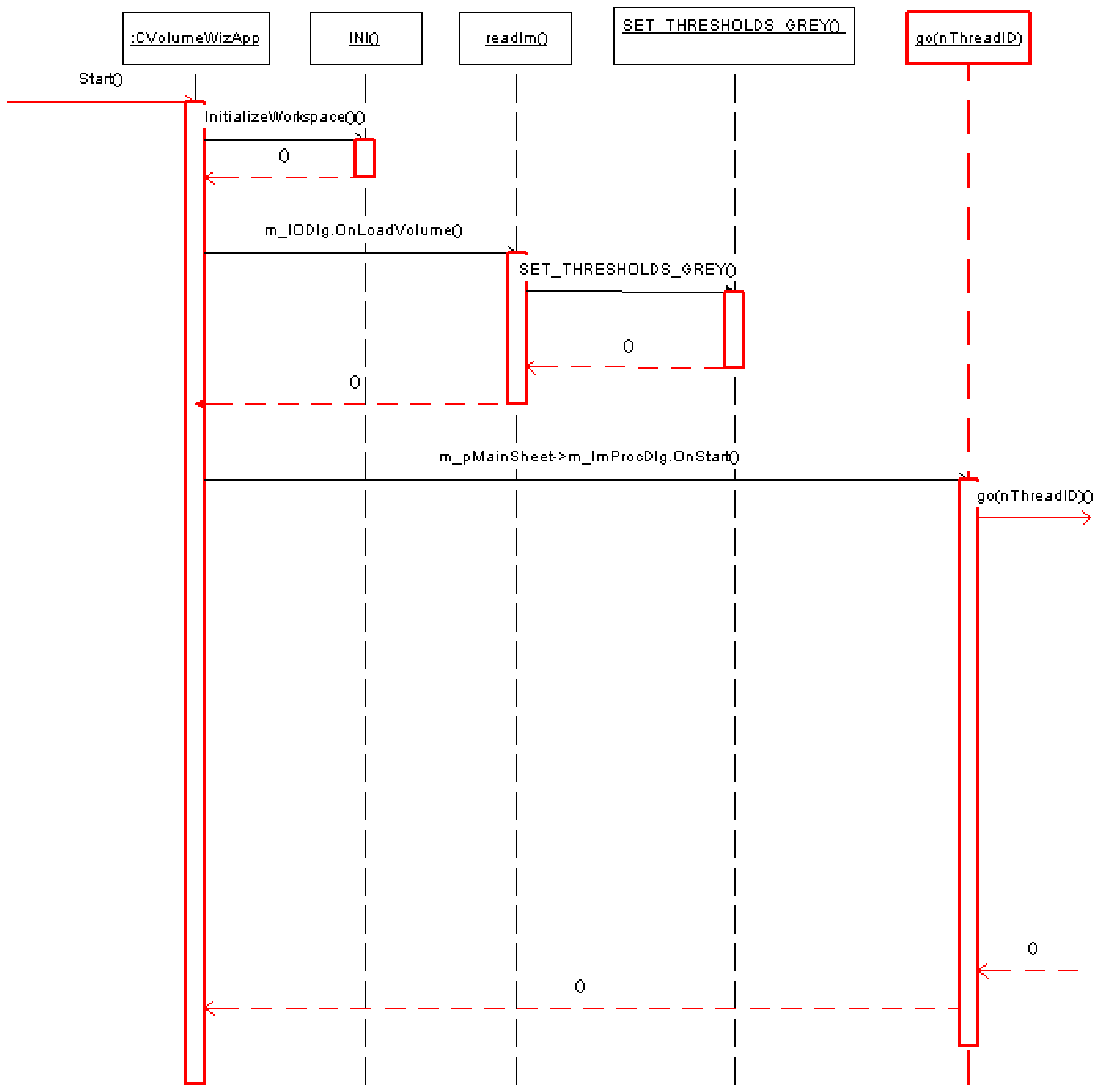

Fig. 34: The algorithm on the previous page as a sequence diagram, this is the first part...

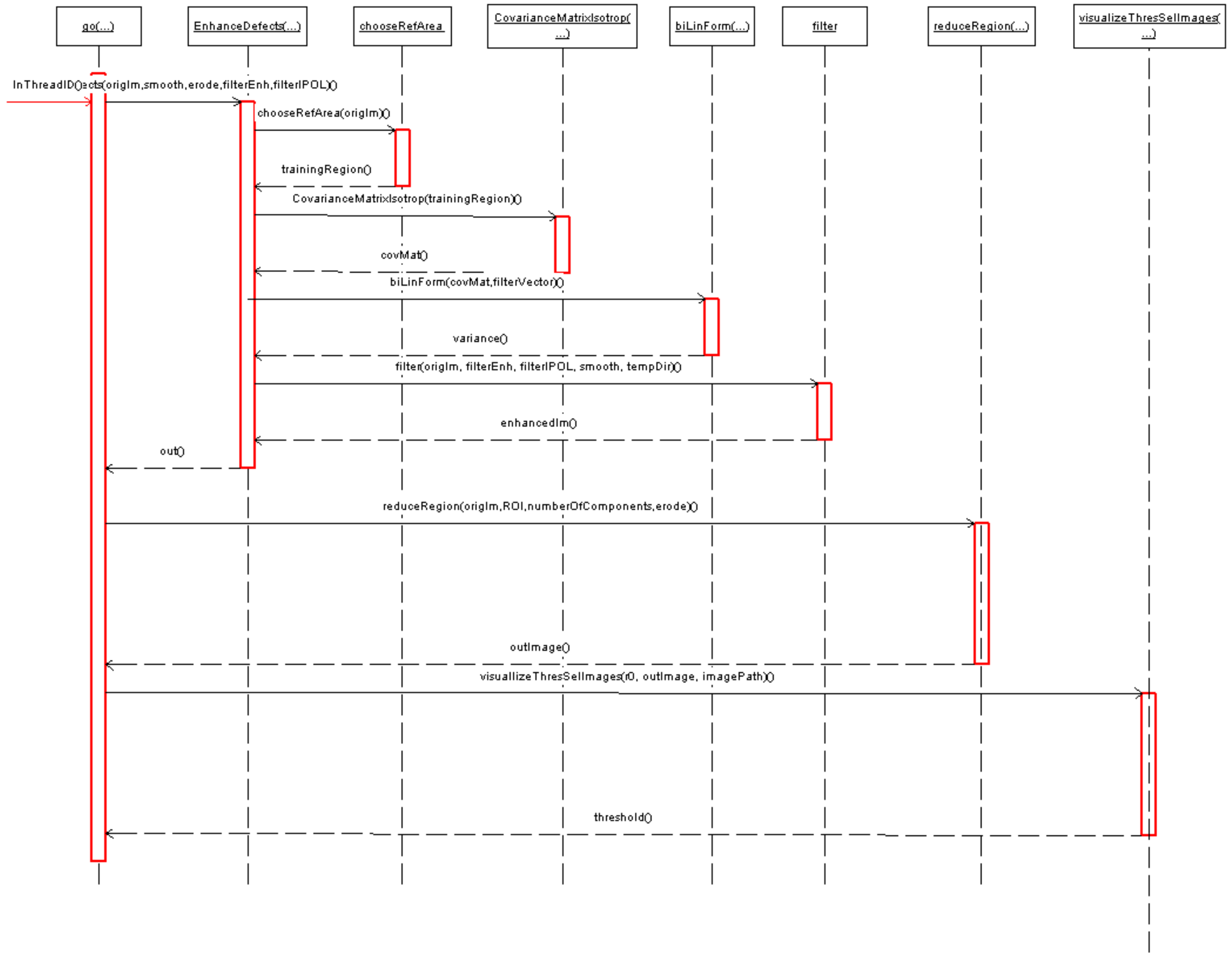
go(...)
EnhanceDefects(...)
chooseRefArea
CovarianceMatrixIsotrop(...)
biLinForm(...)
filter
reduceRegion(...)
visualizeThresSelImages(...)
InThreadIDObjects(origIm,smooth,erode,filterEnh,filterIPOL)()
chooseRefArea(origIm)()
trainingRegion()
CovarianceMatrixIsotrop(trainingRegion)()
covMat()
biLinForm(covMat,filterVector)()
variance()
filter(origIm, filterEnh, filterIPOL, smooth, tempDir)()
enhancedIm()
out()
reduceRegion(origIm,ROI,numberOfComponents,erode)()
outImage()
visuallizeThresSelImages(r0, outImage, imagePath)()
threshold()

Fig. 35: ..., and this is the second part.

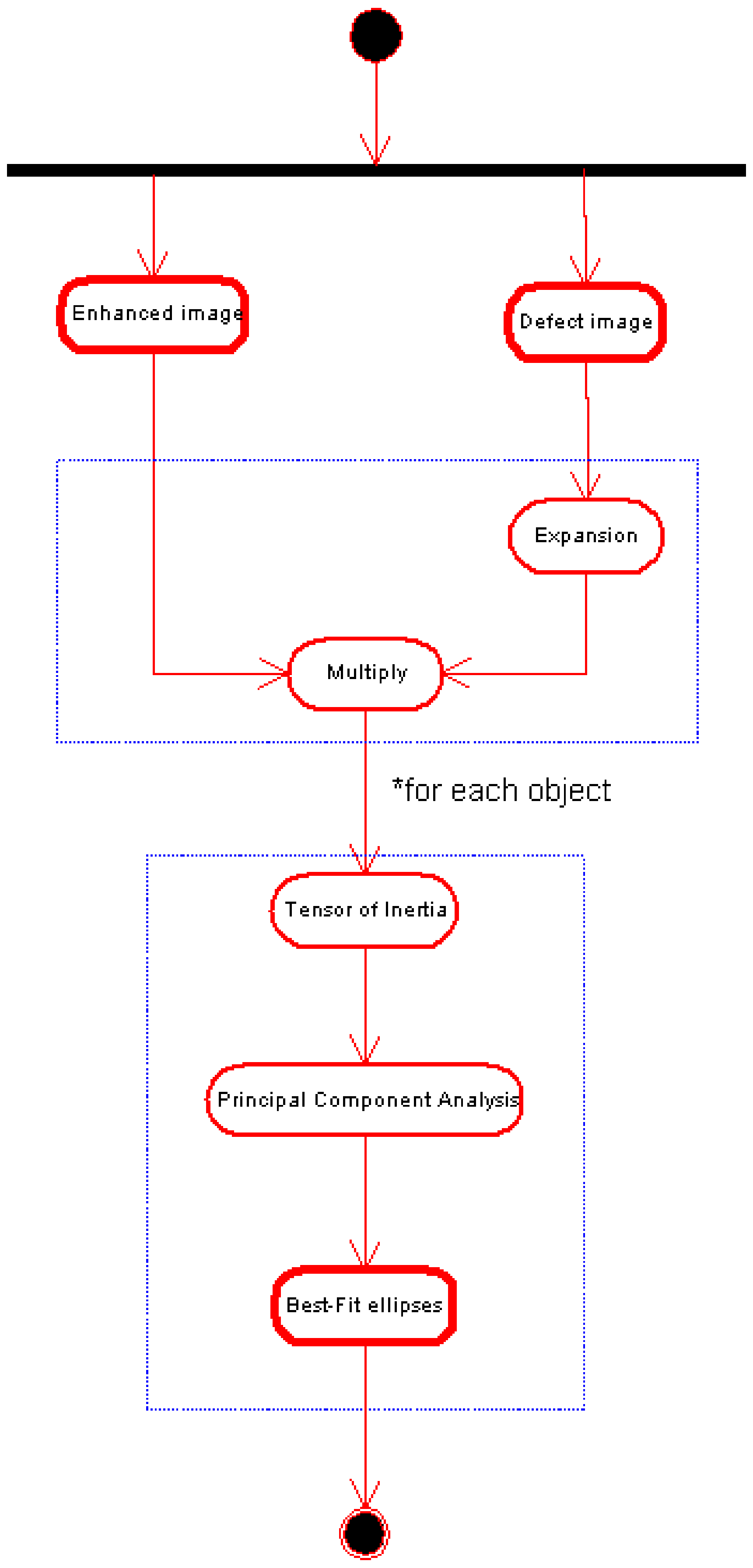

Fig. 36: Fitting ellipses to localized objects (see section 7.1)

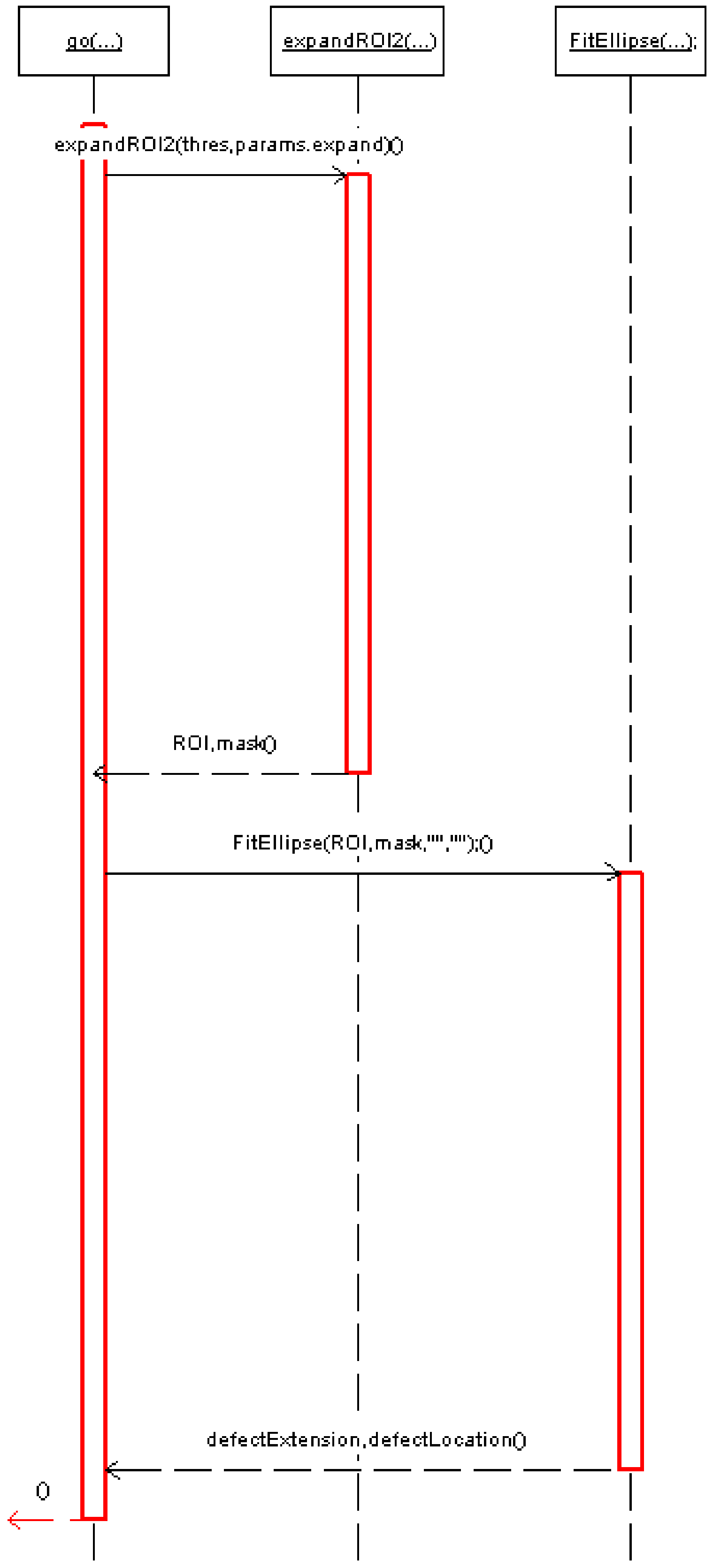
go(...)
expandROI2(...)
FitEllipse(...);
expandROI2(thres,params.expand)()
ROI,mask()
FitEllipse(ROI,mask,"","");()
defectExtension,defectLocation()
0

Fig. 37: The algorithm for fitting ellipses as a sequence diagram.

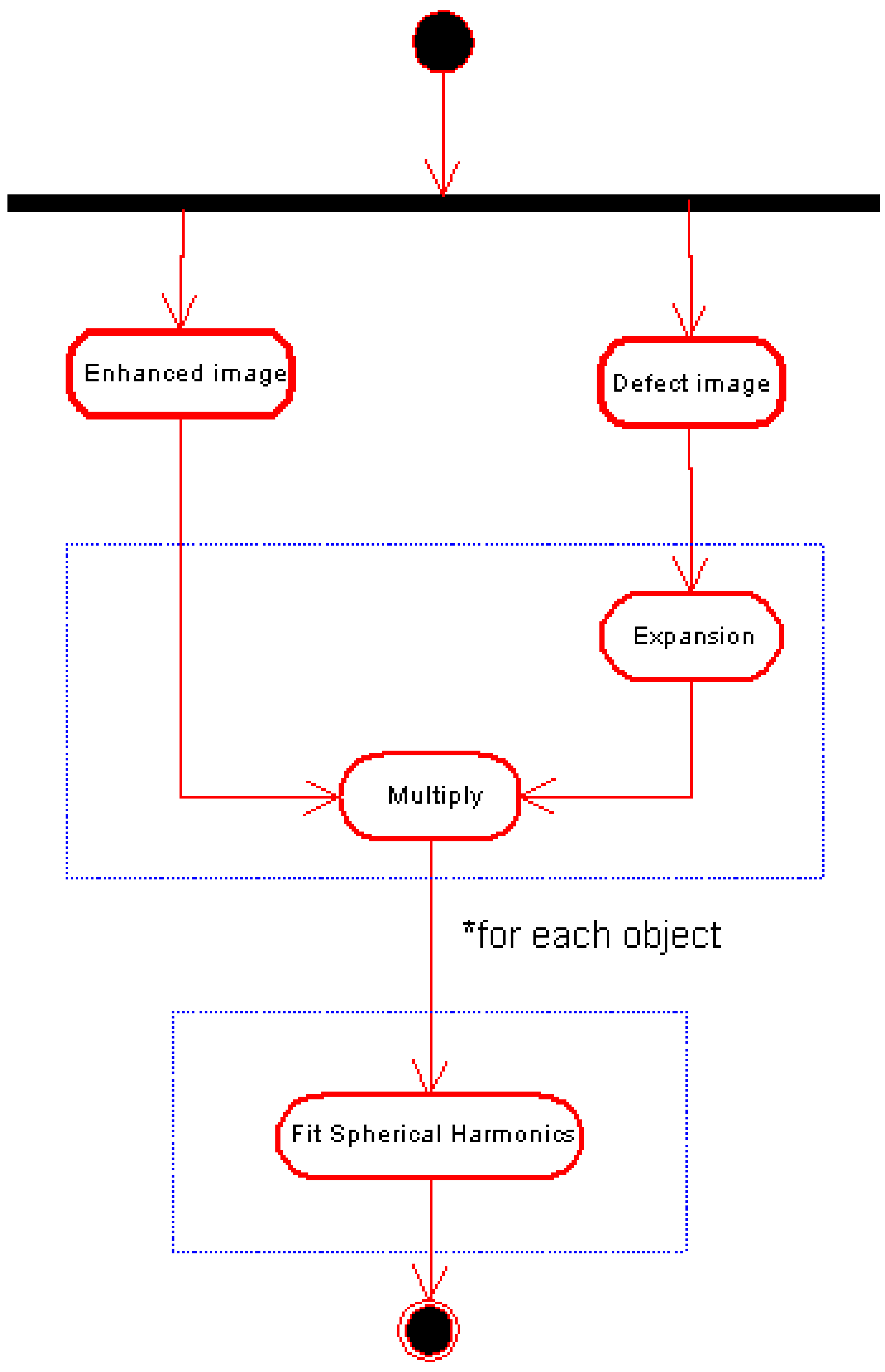

Fig. 38: Object modelling with spherical harmonics (see section 7.2)

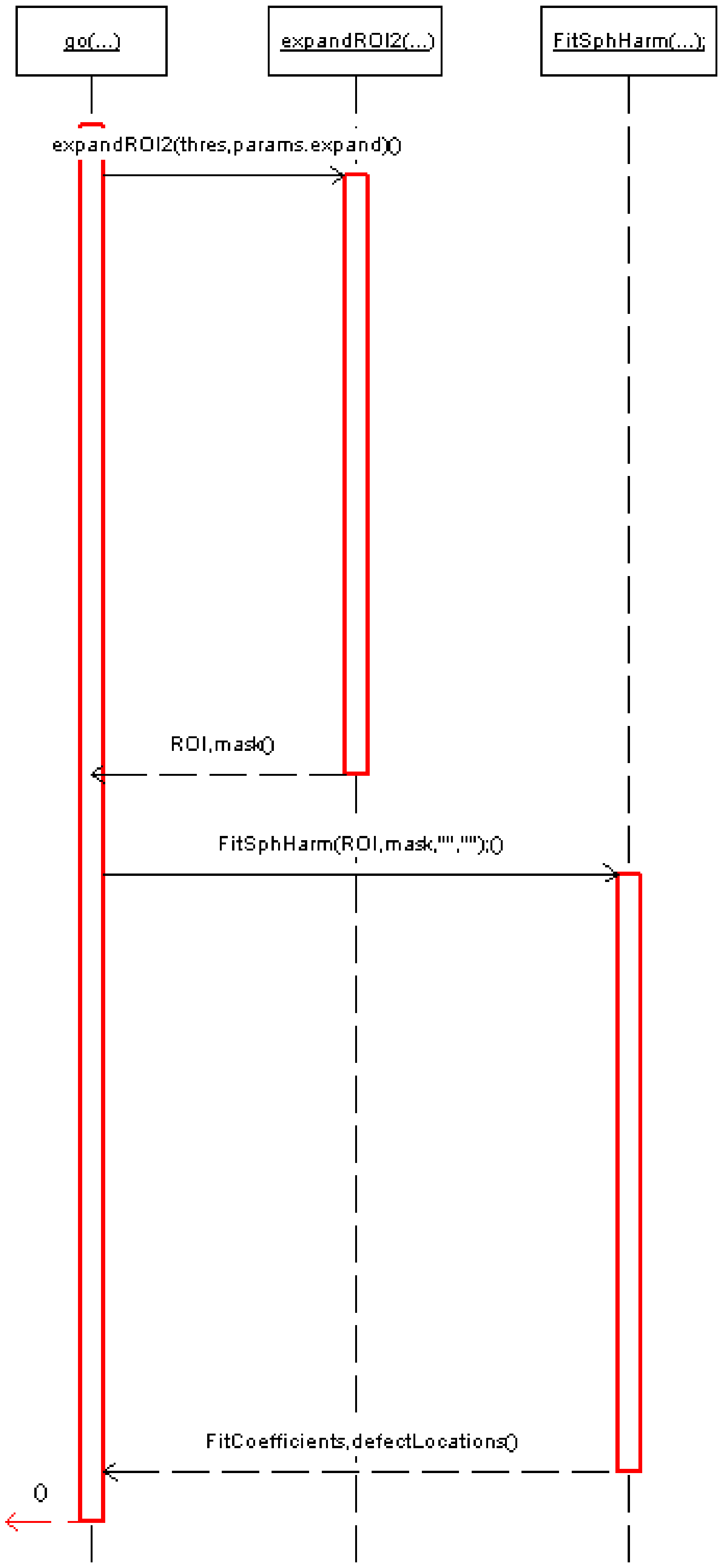
go(...)
expandROI2(...)
FitSphHarm(...);
expandROI2(thres,params.expand)()
ROI,mask()
FitSphHarm(ROI,mask,"","");()
FitCoefficients,defectLocations()
0

Fig. 39: Object modeling with spherical harmonics shown as a sequence diagram

References

1. W. Heinrich. *Automated X-ray inspection of castings in series.* PhD thesis, Institute for Electrical Engineering, Technical University of Berlin, 1988.
2. A. Saya A. Gayer and A. Siloh. Automatic recognition of welding defects in real-time radiography. *Non-Destructive Testing International*, 23(4):131–136, 1990.
3. H. Hecker. *A new method for the evaluation of X-ray images for the automated inspection of castings (In German).* PhD thesis, Institute for Electrical Engineering, Technical University of Berlin, 1995.
4. V. Lashkia. Defect detection in X-ray images using fuzzy reasoning. *Image and Vision Computing*, 19:261–269, 2001.
5. L.A. Feldkamp J.W. Kress and L.C. Davis. Practical conebeam algorithm. *Journal of the Optical Society of America A - Optics Image Science and Vision*, 1(6):612–619, 1984.
6. M. Maisl J. Buck and H. Reiter. The cylinder algorithm. An efficient reconstruction algorithm for the 3D X-ray computed tomography (3D-CT) in NDT. In *Topical Conference on ASNT Industrial Computed Tomography*, pages 89–93, 1996.
7. M. Maisl. *Entwicklung und Aufbau eines hochauflösenden Röntgen-CT Systems.* PhD thesis.
8. D. Sersic and S. Loncaric. Enhancement of mammographic images for detection of microcacifications. In *Proceedings of the IX^{th} European Signal Processing Conference*, volume 2, pages 693–696, 1998.
9. L.M. Myers. Visualization of brain surface features using registered partially segmented MRI scans. In *SPIE Proceedings on Medical Imaging*, volume 2431, pages 43–52. 1995.
10. B. Modayur J. Prothero G. Ojemann K. Maravilla J. Brinkley. Visualization-based mapping of language function in the brain. *Neuroimage*, 6:245–258, 1997.
11. K.C. Fan J.H. Chang and Y.L. Chang. Multi-modal gray-level histogram modeling and decomposition. *Image and Vision Computing*, 20:203–216, 2001.
12. A. Witkin M. Kass and D. Terzopoulos. Snakes: active contour models. In *Proceedings of the first international conference of computer vision*, 1987.
13. F.A. Velasco and J.L. Marroquín. Robust parametric active contours: the sandwich snakes. *Machine Vision and Applications*, 12:238–242, 2001.
14. F. Raisch H. Scharr N. Kirchgešner B. Jähne R.H.A. Fink D. Uttenweiler. Velocity and feature estimation of actin filaments using active contours in noisy flourescence image sequences. In *Proceedings of the 2nd IASTED Conference on Visualization, Imaging and Image Processing (VIIP)*, pages 645–650, 2002.
15. S. Frantz. A new approach to the localization of 3D anatomical point landmarks in medical images based on deformable models. In *Proceedings of the 23rd DAGM symposium*, volume 2191 of *LNCS*, pages 452–459, 2001.
16. D. Saupe and D.V. Vranić. 3D model retrieval with spherical harmonics and moments. In *Proceedings of the 23rd DAGM symposium*, volume 2191 of *LNCS*, pages 69–75, 2001.
17. T. Wang X. Zhuang and P. Zhang. A highly robust estimator through partially likelihood function modeling and its application in computer vision. In *IEEE Trans. on Pattern Analysis and Machine Intelligence*, volume 14(1), pages 121–129. 1987.
18. K. Palaniappan Y. Huang X. Zhuang A.F. Hasler. Robust stereo analysis. In *IEEE Int. Symposium on Computer Vision, Coral Gables, FL*, pages 43–48, Nov. 19-21 1995.
19. P. Meer J. Jolion and S. Batatouche. Robust clustering with application in computer vision. In *IEEE Trans. on Pattern Analysis and Machine Intelligence*, volume 13(8), pages 791–802. 1991.
20. Hagen Spies and Horst Haussecker. Motion. In Bernd Jähne et al., editor, *Handbook of digital image processing*, volume 2, chapter 13, pages 310–392. 1998.
21. G. Tziritas E. Sifakis, I. Grinias. Video segmentation using fast marching and region growing algorithms. *EURASIP Journal on Applied Signal Processing*, 4:379–388, 2002.
22. M. Lhuillier. Efficient dense matching for textured scenes using region growing. In *Proceedings of the 9th British Machine Vision Conference*, 1998.

23. J. Bigün and G.H. Granlund. Optimal detection of linear symmetry. In *Proceedings ICCV'87, London 1987*, pages 433–438, Washington DC, 1987. IEEE, IEEE Computer Society Press.
24. H. Knutsson. Representing local structure using tensors. In *The 6th Scandinavian Conference on Image Analysis*, Oulu, Finland, June 19-22 1989.
25. A.R. Rao and B.G. Schunk. Computing oriented texture fields. In *Proceedings CVPR'89, San Diego, CA*, pages 61–68, Washington, DC, 1989. IEEE, IEEE Computer Society Press.
26. A.R. Rao. *A taxonomy for texture description and identification.* Springer, New York, 1990.
27. H. Scharr. *Optimal operators in Digital Image Processing.* PhD thesis, University of Heidelberg, 2000.
28. Bernd Jähne. *Digital Image Processing*, chapter 11, page 313f. Springer, 2002.